

# Spherical vs. planar: Steering the electronic communication between Ru nanoparticle and single atom to boost the electrocatalytic hydrogen evolution activity both in acid and alkaline

Yongqiang Feng <sup>a,\*</sup>, Weihang Feng <sup>a</sup>, Jing Wan <sup>b</sup>, Junsheng Chen <sup>a</sup>, Hai Wang <sup>a</sup>, Shumu Li <sup>b</sup>, Tianmi Luo <sup>a</sup>, Yuzhu Hu <sup>a</sup>, Chengke Yuan <sup>a</sup>, Liyun Cao <sup>a</sup>, Liangliang Feng <sup>a</sup>, Jie Li <sup>b</sup>, Rui Wen <sup>b</sup>, Jianfeng Huang <sup>a,\*</sup>

<sup>a</sup> School of Materials Science and Engineering, Shaanxi Key Laboratory of Green Preparation and Functionalization for Inorganic Materials, Shaanxi University of Science and Technology, Xi'an 710021, People's Republic of China

<sup>b</sup> Beijing National Laboratory for Molecular Sciences, Laboratory of Molecular Nanostructure and Nanotechnology, Institute of Chemistry, Chinese Academy of Sciences, Beijing 100190, People's Republic China



## ARTICLE INFO

### Keywords:

Hydrogen evolution reaction  
Electrocatalyst  
Fullerene  
Ruthenium  
Charge transfer

## ABSTRACT

Steering the electronic structure of a catalyst has been considered as an effective way to boost the electrocatalytic activity of hydrogen evolution reaction (HER). Herein, a core-shell architecture comprising a Ru nanoparticle (NP) encapsulated into an oxyfullerene-like carbon cage decorated with single-atomic Ru<sub>N</sub><sub>x</sub> species anchored on nitrogen-doped carbon substrate (Ru<sub>NP</sub>@Ru<sub>N</sub><sub>x</sub>-OFC/NC) was constructed. Benefiting from the efficient electronic communication between Ru NP and atomically-distributed Ru site on the carbon cage, the Ru<sub>NP</sub>@Ru<sub>N</sub><sub>x</sub>-OFC/NC exhibited outstanding electrocatalytic performance for HER both in acid and alkaline. Experimental and theoretical results demonstrated that the charge transfer from Ru NP to single-atomic Ru could steer the electronic density of Ru sites and thus facilitate the adsorption of hydrogen and dissociation of water. Resultantly, such charge electronic communication effectively reduced the Gibbs free energy, leading to the improved HER activity. The present work would promote the design and construction of efficient electrocatalysts for energy conversion and storage.

## 1. Introduction

Hydrogen evolution reaction (HER) has been considered as a fundamental process in electrochemical water splitting for clean and sustainable energy, which can be performed both in acidic and alkaline medium at room temperature [1,2]. However, the large-scale utilization of this technology for hydrogen production was prohibited by the high overpotential and sluggish kinetics, especially in the range of large current output [3–6]. It has been established that the HER process involves Volmer-Heyrovsky or Volmer-Tafel pathway [7], where the adsorption Gibbs free energy of hydrogen on the catalyst surface ( $\Delta G_{H^*}$ ) and water dissociation barrier ( $E_a$ ) were vital descriptors associated with the charge-transfer kinetics [8]. Although precious metal Pt-based electrocatalysts exhibit outstanding HER activity both in acidic and alkaline system [3,9], their high cost and low reserve as well as the unfavorable catalytic durability pushed researchers to improve the

performance of Pt-based HER catalysts or pursue variable alternatives with low cost and high efficiency (e.g., transition metal oxides [10,11], nitrides [12,13], carbides [14–16], sulfides [17–19], and phosphides [20–22]). To this end, diverse non-platinum catalysts such as ruthenium (Ru) [23–25], iridium (Ir) [26,27] and rhodium (Rh) [28] have aroused extensive attention in the form of alloys [29–31], nanoparticles (NPs) [32,33] and single atom [7,23,34]. Among this, Ru, one of the platinum group metals, has been proven to be a desirable candidate due to its relatively low cost (4% price of Pt) and high stability, and particularly the  $\Delta G_{H^*}$  of Ru–H bond is close to that of the optimum Pt–H bond at the center of volcanic plot for HER [32,33]. For instance, Mahmood et al. reported an efficient and robust electrocatalyst of Ru NPs dispersed uniformly within a nitrogenated holey two-dimensional carbon structure (Ru@C<sub>2</sub>N) [32], which exhibited outstanding HER performance with small overpotential and excellent stability both in acid and basic electrolyte. To maximize the atomic utilization efficiency, the

\* Corresponding authors.

E-mail addresses: [fengyq@sust.edu.cn](mailto:fengyq@sust.edu.cn) (Y. Feng), [huangjf@sust.edu.cn](mailto:huangjf@sust.edu.cn) (J. Huang).

single-atom catalysts (SACs) have been put forward to the frontier nowadays [35–38]. Ruthenium and nitrogen co-doped carbon nanowires prepared by Lu et al. displayed a much better HER performance than the commercial platinum catalyst, where the atomic  $\text{RuC}_{x}\text{N}_y$  moiety with low hydrogen binding energy and water dissociation barrier was attributed to the superior HER activity [7]. Besides, the synergistic effect between the single atom and NP on the HER activity has been addressed recently since these two components are prone to coexist in one catalyst [39–42]. However, the intrinsic electrochemical active sites for HER process varied from one catalyst to another due to the different geometric configuration and electronic structure of the individual electrocatalyst [39–42]. Therefore, it is urgent and necessary to design and construct more electrocatalysts with unique structures to help further understand the underlying mechanism for HER.

On the other hand, the electrochemical performance of the single atom sites and NPs within a catalyst is highly susceptible to the electronic environment at atomic level [43]. It was found that the Ru–C bonding structure with most stable energy of hydrogen bonding in the catalyst of Ru NP anchored on multiwalled carbon nanotube ( $\text{Ru}@\text{MWCNT}$ ) was the most plausible active site [33]. More recently, Su et al. demonstrated that enhanced charge transfer occurred at the interface of Ru NPs and single metal atoms (e.g., Co, Fe and Ni) doped carbon substrate, resulting in synergistic electronic coupling and optimized  $\Delta G_{\text{H}^*}$  of hydrogen on Ru NPs as well as improved HER performance [41]. Thus, the electronic interaction between the metal species and their surroundings, which sensitively depend on the shape and configuration of the catalyst, played a critical role in regulating the charge distribution and electronic state, and thus controlling the HER performance. Considering one metal NP coupled with a single atom imbedded on a spherical matrix or a plane substrate, the electronic communication between the metal NP and the single atom will be different depend on the distance between them (Fig. S1). In the latter case, the metal NP would be unable to interact with the single atom far away, whereas for the spherical core-shell construction, the inner metal NP could interplay with multiple surrounding single atoms decorated on the shell, resembling the electronic metal-cage interaction (EMCI) of endohedral metallofullerenes (EMFs) [44]. To this respect, it can be envisioned that the maximum utilization of single atom in the EMF analog would boost the electrocatalytic activity.

Inspired by the strong EMCI effect of EMFs, taking Ru as an example, our density functional theory (DFT) calculation result indicate that the EMF-analogous configuration comprising of a Ru NP encapsulated into Ru single-atom decorated fullerene-like carbon cage ( $\text{Ru}_{\text{NP}}@\text{RuN}_4\text{-FC}$ ) exhibit much smaller  $\Delta G_{\text{H}^*}$  and  $E_a$  compared with the Ru NP decorated on Ru-doped planar carbon substrate ( $\text{Ru}_{\text{NP}}\text{-RuN}_4\text{/PC}$ ). The enhanced electronic communication between the Ru NP inside the cage and the single-atomic Ru on the cage can facilitate the adsorption of activated hydrogen and dissociation of water molecule, resulting in improved electrocatalytic performance. To validate this hypothesis experimentally, we design and construct a novel Ru-based hybrid electrocatalyst comprising Ru NP as the core enwrapped by single atomic  $\text{RuN}_x$  species dispersed on oxyfullerene-like carbon cage as the shell anchored on nitrogen-doped carbon matrix ( $\text{Ru}_{\text{NP}}@\text{RuN}_x\text{-OFC/NC}$ ). For comparison, Ru NP coupled with Ru single-atom decorated nitrogen-doped carbon ( $\text{Ru}_{\text{NP}}\text{-RuN}_x\text{/NC}$ ) was also prepared. Impressively, the  $\text{Ru}_{\text{NP}}@\text{RuN}_x\text{-OFC/NC}$  displayed excellent HER activity both in acidic and basic medium with low overpotential (10 mV in 0.5 M  $\text{H}_2\text{SO}_4$  and 19 mV in 1 M KOH at 10 mA  $\text{cm}^{-2}$ ) and superior stability (more than 100 h), much superior to  $\text{Ru}_{\text{NP}}\text{-RuN}_x\text{/NC}$ . On industrial level,  $\text{Ru}_{\text{NP}}@\text{RuN}_x\text{-OFC/NC}$  could deliver a current output of 3000 mA  $\text{cm}^{-2}$  at overpotential of merely 380 and 345 mV in acid and alkaline medium, respectively. This result firmly confirms that the EMF-like configuration could facilitate the electronic communication between the metal core and single atom shell, thus boosting the electrocatalytic activity, which is consistent well with our DFT prediction. Therefore, this work provides a new platform to regulate the electronic structure, activity and stability of

electrocatalysts in the fields of energy conversion and storage.

## 2. Experiment section

### 2.1. Materials

All reagents were used as received without any further purification. Fullerene  $\text{C}_{60}$  was received from Xiamen Funano New Material Technology Co., Ltd. Toluene ( $\text{C}_7\text{H}_8$ ,  $\geq 99.5\%$ ), isopropyl alcohol (IPA,  $(\text{CH}_3)_2\text{CHOH}$ ,  $\geq 99.7\%$ ), ethanol ( $\text{EtOH}$ ,  $\text{CH}_3\text{CH}_2\text{OH}$ ,  $99.7\%$ ), methanol ( $\text{MeOH}$ ,  $\text{CH}_3\text{OH}$ ,  $99\%$ ), tetrabutylammonium hydroxide (TBAH, 50% in water), hydrogen peroxide ( $\text{H}_2\text{O}_2$ , 40%), sulfuric acid ( $\text{H}_2\text{SO}_4$ , 98.5%), copper sulfate pentahydrate ( $\text{CuSO}_4\cdot 5\text{H}_2\text{O}$ ,  $\geq 99\%$ ) were purchased from Sinopharm Chemical Reagent Co., Ltd. Melamine ( $\text{C}_3\text{H}_6\text{N}_6$ ,  $\geq 99.5\%$ ), potassium thiocyanate (KSCN, 99%), ethylene diamine tetra-acetic acid (EDTA, 99.5%), ruthenium trichloride ( $\text{RuCl}_3$ , 99%), Pt/C (20 wt%), iridium oxide ( $\text{IrO}_2$ , 99%), Nafion solution (5%) and potassium hydroxide (KOH,  $\geq 85\%$ ) were purchased from Sigma-Aldrich. The hydrophilic carbon paper (CP) were purchased from Suzhou Sinero Technology Co., Ltd. Deionized water (DW,  $18.25\text{ M}\Omega/\text{cm}$ ) was obtained from the ultra-pure purification system (ULUPURE, UPDR-I-10T).

### 2.2. Instrument and characterization

X-ray diffraction (XRD) patterns of the electrocatalysts were tested on a Rigaku D/max-2200PC diffractometer (Japan) with  $\text{Co K}\alpha$  radiation. High-resolution transmission electron microscope (HRTEM) images were recorded using a JEOL JEM-2010 field-emission transmission electron microscope with an accelerating voltage of 200 kV. The high-angle annular dark-field scanning transmission electron microscopy (HAADF-STEM) images were obtained by using a Themis Z/ORION70-4 M scanning/transmission electron microscope operated at 300 kV, equipped with a probe spherical aberration corrector. Inductively coupled plasma-atomic emission spectroscopy (ICP-AES) was executed on a SHIMADZU ICPE-90000 instrument. The atomic force microscopy (AFM) experiments were performed by using an AFM (Bruker Corp., Dimension Icon) situated in an Ar-filled glovebox ( $\text{H}_2\text{O} < 0.1\text{ ppm}$ ,  $\text{O}_2 < 0.1\text{ ppm}$ ). AFM images was achieved by using a silicon AFM probe ( $k = 26\text{ N/m}$ ,  $f_0 = 300\text{ kHz}$ ) with a scan rate of 0.854 Hz (about 5 min for each image) in the mode of peakforce quantitative nano mechanics (Peak-Force QNM). Matrix-assisted laser desorption ionization time of flight-mass spectrum (MALDI-TOF-MS) was performed on Bruker UltraFlex instrument. X-ray synchrotron radiation was acquired on the B14W beamline in Shanghai Synchrotron Radiation Facility. Fourier transform extended X-ray absorption fine structure (FT-EXAFS) shell fitting was carried out with Artemis Software. X-ray photoelectron spectroscopy (XPS) measurements were performed on a Thermo VG ESCALAB 250 X-ray photoelectron spectrometer with  $\text{Al K}\alpha$  radiation at a pressure of about  $2 \times 10^{-9}\text{ Pa}$ . The chemical bonding states and compositions of the samples were investigated by Fourier transform infrared spectroscopy (FT-IR) in the range of  $4000\text{--}400\text{ cm}^{-1}$  on a Nicolet-5700 spectrometer. Raman spectra were collected on a Renishaw-invia microscopic confocal laser Raman spectrometer with 532 nm as the excitation laser. The pyrolysis process of the samples was characterized by thermogravimetry and differential thermal analysis (TG/DTA) from room temperature to 1000 °C in  $\text{N}_2$  or air atmosphere with a heating rate of  $5\text{ }^{\circ}\text{C min}^{-1}$  on a thermal analyzer (DTA-50). The thermogravimetry-mass spectrum (TG-MS) was conducted on a SETARAM LABSYS machine (LABSYS EVO, France) equipped with a TILON (T2000) instrument for the mass detection. The electrochemical performance was tested on a CHI660E workstation (Chenhua, Shanghai).

### 2.3. Synthesis of $\text{C}_{60}(\text{OH})_n$

The  $\text{C}_{60}(\text{OH})_n$  was prepared with a modified procedure according to the literature [45], details can be found in the supporting information.

## 2.4. Synthesis of $\text{Ru}_{\text{NP}}@\text{RuN}_x\text{-OFC/NC}$

The precursor of  $\text{Ru-C}_{60}(\text{OH})_n/\text{NC}$  was prepared by hydrothermal treatment of the mixture of  $\text{RuCl}_3$  (1 mmol) and melamine (1 g) in the presence of 40 mg  $\text{C}_{60}(\text{OH})_n$  dissolving in 25 ml of water under  $180^\circ\text{C}$  for 12 h. Then the as-prepared  $\text{Ru-C}_{60}(\text{OH})_n/\text{NC}$  was carbonized under  $\text{Ar}/\text{H}_2$  (5%) flow in a tube furnace at  $600^\circ\text{C}$  for 2 h with a raising rate of  $5^\circ\text{C min}^{-1}$ . After cooling to room temperature, the deep-black powder was collected, defined as  $\text{Ru}_{\text{NP}}@\text{RuN}_x\text{-OFC/NC}$ . For comparison,  $\text{Ru}_{\text{NP}}\text{-RuN}_x/\text{NC}$  was synthesized via the same experimental condition without addition of  $\text{C}_{60}(\text{OH})_n$ .  $\text{Ru}_{\text{SA}}/\text{NC}$  and  $\text{Ru}_{\text{NP}}/\text{NC}$  were also prepared for comparison, details can be found in the [supporting information](#).

## 2.5. Electrochemical measurement

The HER properties were performed on CHI660E electrochemical workstation using a three-electrode system in Ar-saturated 0.5 M  $\text{H}_2\text{SO}_4$  or 1 M KOH aqueous solution. A glassy carbon electrode (GCE,  $\phi = 3$  mm), a graphite rod and a saturated calomel electrode (SCE) were used as working electrode, counter electrode and reference electrode, respectively. The working electrode was prepared as follow: Firstly, 5 mg of catalyst powder was dispersed in 298  $\mu\text{L}$  of IPA and 2  $\mu\text{L}$  of Nafion under ultra-sonication to form a homogenous ink, then ca. 2  $\mu\text{L}$  of the ink was drop-casted on the surface of GCE and dried at room temperature. For the large-scale current measurement, the catalyst ink was drop-casted on the surface of carbon paper with a loading amount of 0.37  $\text{mg cm}^{-2}$ .

The SCE reference electrode was calibrated against the reversible hydrogen potential (RHE) in  $\text{H}_2$ -saturated 0.5 M  $\text{H}_2\text{SO}_4$  or 1 M KOH with Pt plate as the working electrode and Pt wire as the counter electrode [\[46\]](#). Therefore, the potentials in the present work can be obtained by the following equations:

$$E(\text{RHE}) = E(\text{SCE}) + 0.266 \text{ (0.5 M H}_2\text{SO}_4) \quad (1)$$

$$E(\text{RHE}) = E(\text{SCE}) + 1.047 \text{ (1 M KOH)} \quad (2)$$

The linear scanning voltammetry (LSV) curve was recorded in a  $\text{N}_2$ -saturated 0.5 M  $\text{H}_2\text{SO}_4$  or 1 M KOH with a scan rate of  $1 \text{ mV s}^{-1}$ . Tafel slope was obtained by plotting the LSV curve using the equation of  $\eta = a + b \log j$ , where  $\eta$  refers to the overpotential,  $b$  is the Tafel slope and  $a$  denotes the intercept [\[47\]](#). The electrochemical impedance spectroscopy (EIS) tests were performed in the frequency range from 100 kHz to 0.1 Hz with an amplitude of 5 mV. To obtain the double-layer capacitor ( $C_{\text{dl}}$ ) data, cyclic voltammetry (CV) curves were collected in the non-Faradic region with scanning rate of 2, 4, 6, 8, 10 and  $12 \text{ mV s}^{-1}$ , and the  $C_{\text{dl}}$  could be obtained by plotting the current difference ( $\Delta j$ ) against the scanning rate. The electrochemical active surface area (ECSA) was estimated by the equation of  $\text{ECSA} = C_{\text{dl}} / C_s \times S$ , where  $C_s$  refers to the specific capacitance on the electrode surface and  $S$  is the surface area of the electrode [\[4\]](#). Long-term current-time tests were recorded by taking a chronoamperometric curve. All the electrochemical tests were tested at room temperature.

The underpotential deposition (UPD) of copper (Cu) was used to figure out the active sites of the  $\text{Ru}_{\text{NP}}@\text{RuN}_x\text{-OFC/NC}$ . In this approach, the number of active sites ( $n$ ) can be qualified based on the UPD copper stripping charge ( $Q_{\text{Cu}}\text{, Cu}_{\text{upd}} \rightarrow \text{Cu}^{2+} + 2\text{e}^-$ ) with the following equation of  $n = Q_{\text{Cu}} / 2 \text{ F}$ , where  $F$  is the Faraday constant ( $96,485.3 \text{ C mol}^{-1}$ ) [\[32\]](#). The turnover frequency (TOF) can be calculated following the equation of  $\text{TOF} = I / (2nF)$ , where  $I$  is the current (A) and the factor 1/2 is based on the consideration that two electrons are transferred to form one hydrogen molecule.

The overall water splitting was conducted on a two-electrode setup with a scan rate of  $3 \text{ mV s}^{-1}$  under 1 M KOH. For comparison, a water electrolyzer cell of  $\text{IrO}_2\text{||Pt/C}$  was also fabricated using 5 mg of  $\text{IrO}_2$  and 5 mg of 20% Pt/C as the cathode and anode, respectively.

## 2.6. Theoretical calculation

All the calculations were performed within the framework of DFT as implemented in the Vienna Ab initio Software Package (VASP 5.3.5) code within the Perdew–Burke–Ernzerhof (PBE) generalized gradient approximation and the projected augmented wave (PAW) method [\[48–51\]](#). The cutoff energy for the plane-wave basis set was set to 400 eV. Four different structures were considered in this calculation, including  $\text{RuN}_4$  single atom, small Ru-cluster composed of 6 atoms, co-effect of Ru single atom and small Ru-cluster structure imbedded onto the surface of planar carbon matrix and core-shell structure of Ru cluster encapsulated into  $\text{RuN}_4$ -decorated carbon cage. All structures were first optimized to reach their most stable configuration. During the geometry optimizations, all the atom positions were allowed to relax. The Brillouin zone of the surface unit cell was sampled by Monkhorst–Pack (MP) grids for catalyst structure optimizations [\[52\]](#). The catalyst surface was determined by  $1 \times 1 \times 1$  Monkhorst–Pack grid. The convergence criterion for the electronic self-consistent iteration and force was set to  $10^{-5} \text{ eV}$  and  $0.01 \text{ eV}/\text{\AA}$ , respectively. The climbing image nudged elastic band (CI-NEB) method was used to confirm the transition states with only one imaginary frequency along the reaction coordinates [\[53,54\]](#). The adsorption energy ( $E_{\text{ads}}$ ) of the surface species is defined by:

$$E_{\text{ads}} = E_{\text{total}} - E_{\text{surface}} - E_{\text{species}}, \quad (3)$$

where  $E_{\text{total}}$  represents the total energy of the adsorbed species with catalyst surface,  $E_{\text{surface}}$  is the energy of the empty surface, and  $E_{\text{species}}$  is the energy of the species in the gas phase.

The activation barrier ( $E_a$ ) and reaction energy ( $E_r$ ) are defined by:

$$E_a = E_{\text{TS}} - E_{\text{IS}} \quad (4)$$

$$E_r = E_{\text{FS}} - E_{\text{IS}} \quad (5)$$

where  $E_{\text{TS}}$  represents the energy of transition state,  $E_{\text{IS}}$  represents the energy of initial state, and  $E_{\text{FS}}$  represents the energy of final state.

## 3. Results and discussion

### 3.1. DFT calculation

The conception was firstly investigated by DFT calculation. As shown in [Fig. 1](#), Ru NP was encapsulated into a fullerene-like carbon cage, on which a single-atomic  $\text{RuN}_4$  species was decorated ( $\text{Ru}_{\text{NP}}@\text{RuN}_4\text{-FC}$ ), forming a configuration analogous to EMF ([Fig. 1a](#)). Besides, a reference structure with Ru NP located on the surface of planar carbon matrix doped with  $\text{RuN}_4$  moiety ( $\text{Ru}_{\text{NP}}\text{-RuN}_4\text{/PC}$ ) was built for comparison ([Fig. 1b](#)). As depicted in [Fig. 1c](#), the electronic density of state (DOS) of  $\text{Ru}_{\text{NP}}@\text{RuN}_4\text{-FC}$  possessed a lower  $d$ -band center of  $-3.75 \text{ eV}$  compared to that of  $\text{Ru}_{\text{NP}}\text{-RuN}_4\text{/PC}$  ( $-2.78 \text{ eV}$ ). According to the  $d$ -band center theory, the lower  $d$ -band center ( $\varepsilon_d$ ) refers to more occupancy of anti-bonding state, giving rise to weaker but more favorable bonding strength of hydrogen for hydrogen generation [\[39\]](#). Therefore, the EMF-like  $\text{Ru}_{\text{NP}}@\text{RuN}_4\text{-FC}$  would be more thermodynamically desirable for the  $\text{H}^+$  desorption in HER process. Moreover, the EMF-like  $\text{Ru}_{\text{NP}}@\text{RuN}_4\text{-FC}$  exhibited an optimal  $\Delta G_{\text{H}^+}$  of  $-0.02 \text{ eV}$ , much lower than that ( $0.22 \text{ eV}$ ) of  $\text{Ru}_{\text{NP}}\text{-RuN}_4\text{/PC}$  ([Fig. 1d](#)), indicating an energy-saving process for the hydrogen adsorption. Further Bader charge analysis revealed that the charge transferred from the Ru nanocluster to the Ru single atom was 2.45 and 0.53 e for  $\text{Ru}_{\text{NP}}@\text{RuN}_4\text{-FC}$  and  $\text{Ru}_{\text{NP}}\text{-RuN}_4\text{/PC}$ , respectively, leading to a more active single-atom Ru on the cage in  $\text{Ru}_{\text{NP}}@\text{RuN}_4\text{-FC}$ . Our DFT calculation results signify that the electronic communication between Ru NP and Ru single atom enable to promote the hydrogen adsorption, which in turn would boost the HER activity.

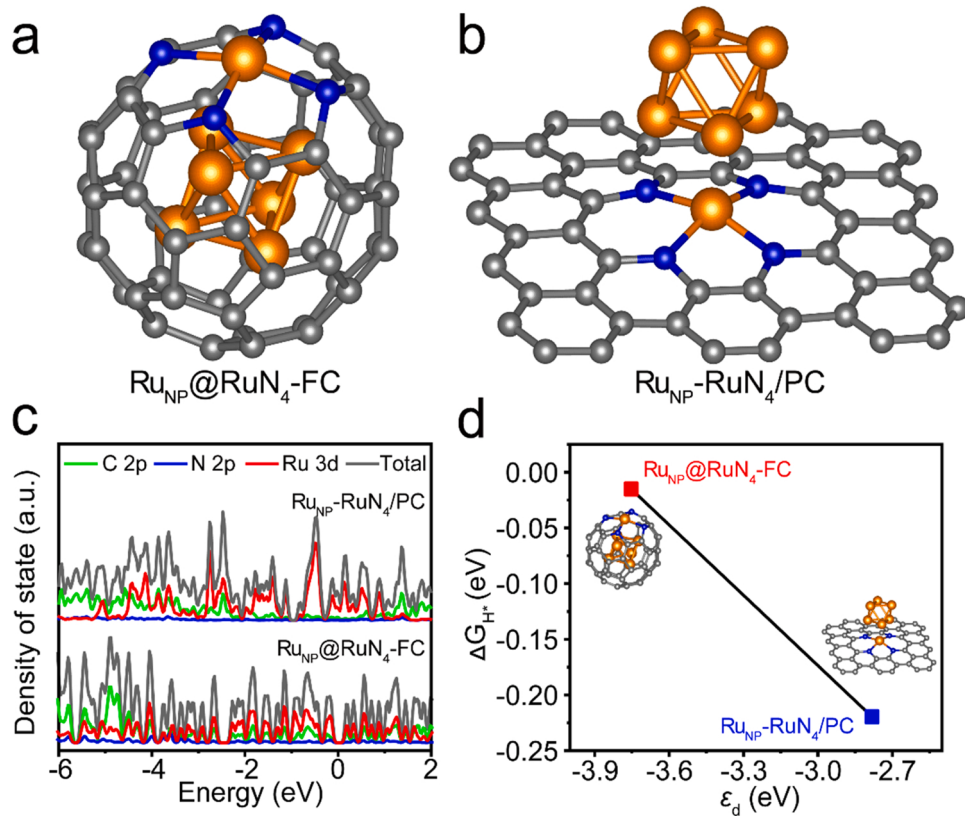


**Fig. 1.** Structure and electronic state of Ru<sub>NP</sub>@RuN<sub>4</sub>-FC and Ru<sub>NP</sub>-RuN<sub>4</sub>/PC. Optimized structure of (a) Ru<sub>NP</sub>@RuN<sub>4</sub>-FC and (b) Ru<sub>NP</sub>-RuN<sub>4</sub>/PC. Color code: Ru gold, N blue and C gray. (c) Density of state diagram of Ru<sub>NP</sub>@RuN<sub>4</sub>-FC and Ru<sub>NP</sub>-RuN<sub>4</sub>/PC. (d) Relationship of hydrogen adsorption Gibbs free energy ( $\Delta G_H^\circ$ ) against the d band center ( $\epsilon_d$ ) of the Ru atoms in Ru<sub>NP</sub>@RuN<sub>4</sub>-FC and Ru<sub>NP</sub>-RuN<sub>4</sub>/PC.

### 3.2. Synthesis and structure characterization

To verify the result predicted by DFT calculation, Ru<sub>NP</sub>@RuN<sub>4</sub>-FC analog material was fabricated by a simple method. Briefly, Ru<sup>3+</sup> ions were coordinated with fullerol in the presence of melamine, followed by thermal pyrolysis under Ar/H<sub>2</sub> atmosphere at elevated temperature according to the TGA measurement (Fig. S2). As schematically illustrated in Fig. 2a, the buckybowl fragments derived from the decomposed fullerol cage (Fig. S2b) reassembled to oxyfullerene-like carbon cage and the Ru<sup>3+</sup> ions tended to aggregate as nanoparticle core and dispersed on the cage shell with nitrogen generated by melamine, defined as Ru<sub>NP</sub>@RuN<sub>x</sub>-OFC/NC. The XRD pattern of the Ru<sub>NP</sub>@RuN<sub>x</sub>-OFC/NC (Fig. 2b) showed Bragg peaks at 44.88°, 49.36°, and 51.57°, corresponding to the (100), (002) and (101) planes of hexagonal Ru (JCPDS No: 06-0663) [43]. The broad peak around 30° was assigned to the melamine-derived graphitic carbon [14], which was also observed in the Ru<sub>SA</sub>/NC and Ru<sub>NP</sub>/NC (Fig. S3). Notably, the peaks belong to Ru<sub>NP</sub>@RuN<sub>x</sub>-OFC/NC was slightly upshifted, which may be caused by the core-shell interaction between the Ru NP and atomic RuN<sub>x</sub> species on the fullerene-like carbon cage. Besides, the Raman spectra of Ru<sub>NP</sub>@RuN<sub>x</sub>-OFC/NC displayed in Fig. 2c exhibited the D and G bands at 1350 and 1583 cm<sup>-1</sup> [55], respectively. The intensity ratio of I<sub>D</sub>/I<sub>G</sub> in Ru<sub>NP</sub>@RuN<sub>x</sub>-OFC/NC was 0.94, a little smaller than that of Ru<sub>NP</sub>-RuN<sub>x</sub>/NC (1.01), indicative of a higher graphitization of Ru<sub>NP</sub>@RuN<sub>x</sub>-OFC/NC. In addition, the C-O stretching vibration in the FTIR spectrum of Ru<sub>NP</sub>@RuN<sub>x</sub>-OFC/NC (Fig. S4) could be attributed to the oxygen atoms bonded to the fullerene-like carbon shell [45]. TEM images disclosed that the core-shell structural Ru<sub>NP</sub>@RuN<sub>x</sub>-OFC was uniformly distributed on the carbon matrix with a statistic average size of 2.5 nm in diameter (Fig. 2d and S5). It was worth noting that the Ru NP was enveloped by a carbon shell with a thickness of ca. 0.32 ~ 0.54 nm (Fig. S6), which could not be observed in the case of Ru<sub>NP</sub>-RuN<sub>x</sub>/NC

(Fig. S7), revealing that the carbon shell was formed by reassembly of the buckybowl fragments derived from the fullerol. Aberration-corrected high-angle annular dark-field scanning TEM (AC-HAADF-STEM) was then applied to acquire the atomic resolution information of Ru<sub>NP</sub>@RuN<sub>x</sub>-OFC/NC. As shown in Fig. 2e, three typical lattice fringes with interplanar distances of 0.203 (I), 0.213 (II) and 0.234 nm (III), corresponding to the (101), (002) and (100) crystal planes of hexagonal Ru, were apparently appeared in the core of Ru NP in Ru<sub>NP</sub>@RuN<sub>x</sub>-OFC/NC, which was well consistent with the XRD result. The distinct lattice fringes observed in different particles would be caused by the random orientation of the Ru NP encapsulated inside the spherical carbon shell. Selected area electron diffraction (SAED) pattern further confirmed the crystal phase of the inner core of Ru NP (Fig. S8). Evidently, a large number of bright spots marked by red arrows denoted the single atom of Ru species in Ru<sub>NP</sub>@RuN<sub>x</sub>-OFC/NC (Fig. 2e and S9), which was atomically dispersed dominantly in the surroundings of the core of Ru NP. A closer inspection of the position analysis revealed that the typical distance between the dispersed single Ru atom randomly selected and the core of Ru NP was determined to be ca. 0.445 nm (yellow circles in Fig. 2e and f), demonstrating that the single atomic Ru species were indeed located on the fullerene-like carbon shell. AFM image and the corresponding height diagram of Ru<sub>NP</sub>@RuN<sub>x</sub>-OFC/NC revealed that the newly-formed fullerene-like carbon cage was a bit larger than that of the C<sub>60</sub>(OH)<sub>n</sub> precursor (Fig. 2g and Fig. S10), which was further verified by the MALDI-TOF-MS analysis (Fig. S11). Elemental mapping of Ru<sub>NP</sub>@RuN<sub>x</sub>-OFC/NC (Fig. 2h) and Ru<sub>NP</sub>-RuN<sub>x</sub>/NC (Fig. S12) displayed that all the elements including Ru, N, C and O were evenly distributed over the entire sample. ICP-AES analysis combined with TGA result (Fig. S13) of Ru<sub>NP</sub>@RuN<sub>x</sub>-OFC/NC unveiled that the Ru content in Ru<sub>NP</sub>@RuN<sub>x</sub>-OFC/NC was higher (17.84%) than that of Ru<sub>NP</sub>-RuN<sub>x</sub>/NC (15.36%), which could be attributed to enwrapped single atom Ru species on the surface of Ru NP.

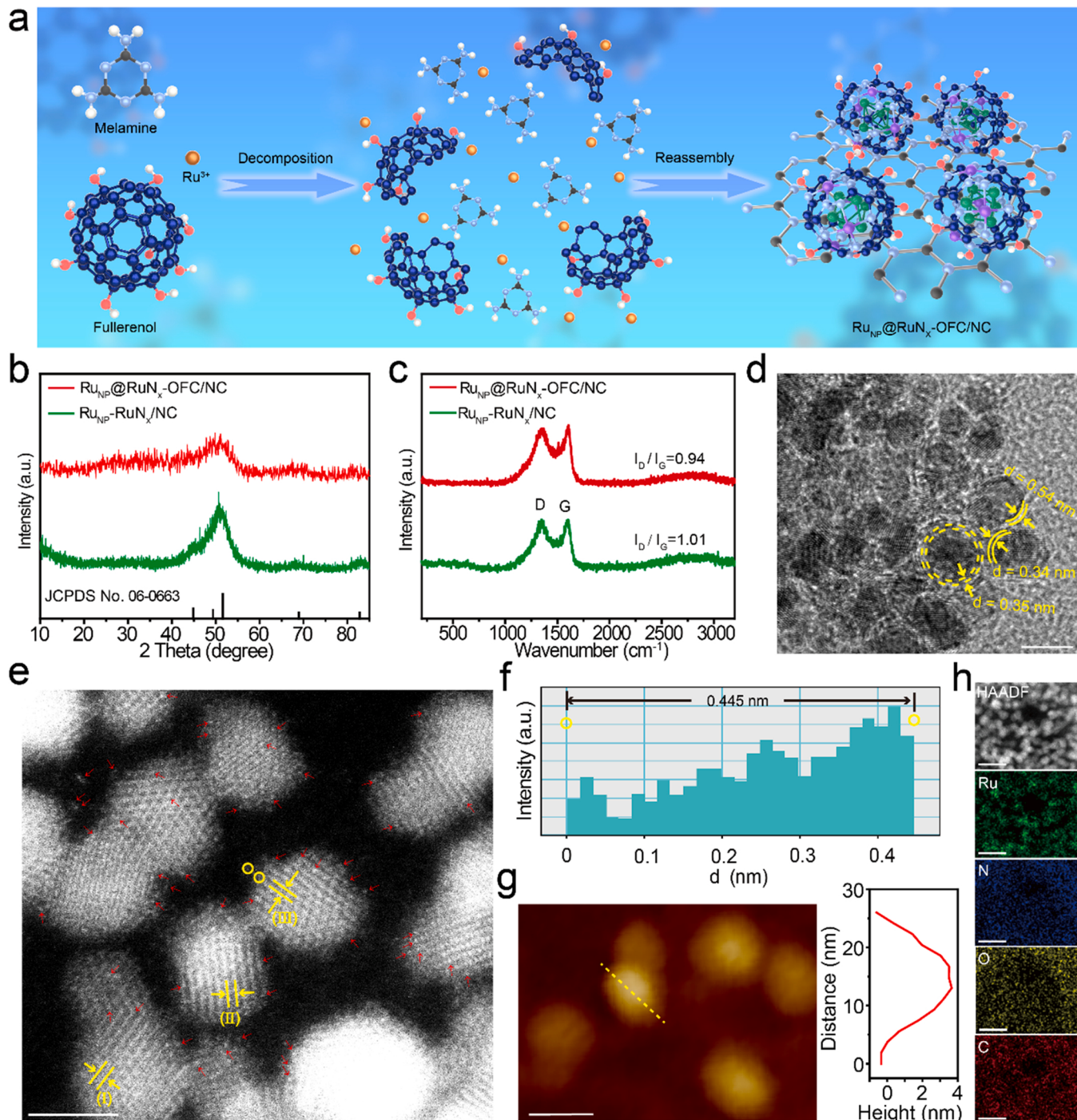


**Fig. 2.** Structure characterization of  $\text{Ru}_{\text{NP}}@\text{RuN}_x\text{-OFC/NC}$ . (a) Schematic illustration of the formation process of  $\text{Ru}_{\text{NP}}@\text{RuN}_x\text{-OFC/NC}$ . (b) XRD patterns and (c) Raman spectra of  $\text{Ru}_{\text{NP}}@\text{RuN}_x\text{-OFC/NC}$  (red) and  $\text{Ru}_{\text{NP}}\text{-RuN}_x\text{/NC}$  (green). (d) HRTEM and (e) AC-HAADF-STEM images of  $\text{Ru}_{\text{NP}}@\text{RuN}_x\text{-OFC/NC}$ . The yellow dashed circle and solid line in d indicate the core-shell structure of  $\text{Ru}_{\text{NP}}@\text{RuN}_x\text{-OFC/NC}$  and the thickness of the carbon shell. The red arrows in e denote the single-atom Ru on the surface of the spherical  $\text{Ru}_{\text{NP}}@\text{RuN}_x\text{-OFC/NC}$ . (f) Spatial distance of the two single atoms marked by yellow circles in e. (g) AFM image (left panel) and height diagram (right panel) of  $\text{Ru}_{\text{NP}}@\text{RuN}_x\text{-OFC/NC}$ . (h) HAADF image of  $\text{Ru}_{\text{NP}}@\text{RuN}_x\text{-OFC/NC}$  and the corresponding elemental mapping for Ru, N, O and C. Scale bars in d, e, g and h are 5, 2, 20 and 10 nm, respectively.

To further determine the chemical coordination states and electronic structures of Ru species, X-ray absorption spectroscopy (XAS) measurements including X-ray absorption near-edge structure (XANES) spectrum and extended X-ray absorption fine structure (EXAFS) were performed. Fig. 3a shows the Ru K-edge XANES spectra of  $\text{Ru}_{\text{NP}}@\text{RuN}_x\text{-OFC/NC}$ ,  $\text{Ru}_{\text{NP}}\text{-RuN}_x\text{/NC}$ , Ru foil and  $\text{RuO}_2$ . It can be seen that the absorption edge of  $\text{Ru}_{\text{NP}}@\text{RuN}_x\text{-OFC/NC}$  is close to that of Ru foil but remarkably different from that of  $\text{RuO}_2$ , indicating that metallic Ru NP

was dominant in  $\text{Ru}_{\text{NP}}@\text{RuN}_x\text{-OFC/NC}$ . In addition, in the range of 22130–22160 eV, the  $\text{Ru}_{\text{NP}}@\text{RuN}_x\text{-OFC/NC}$  showed an almost flat feature, corresponding to the combined contributions of Ru NPs and single atoms [7]. The Fourier transform (FT) EXAFS curves of the  $\text{Ru}_{\text{NP}}@\text{RuN}_x\text{-OFC/NC}$ ,  $\text{Ru}_{\text{NP}}\text{-RuN}_x\text{/NC}$ , Ru foil and  $\text{RuO}_2$  were depicted in Fig. 3b. It was obvious that  $\text{Ru}_{\text{NP}}@\text{RuN}_x\text{-OFC/NC}$  showed one prominent coordination peak at 2.35 Å along with a small shoulder at 1.92 Å similar to that in Ru foil, which could be ascribed to the Ru-Ru

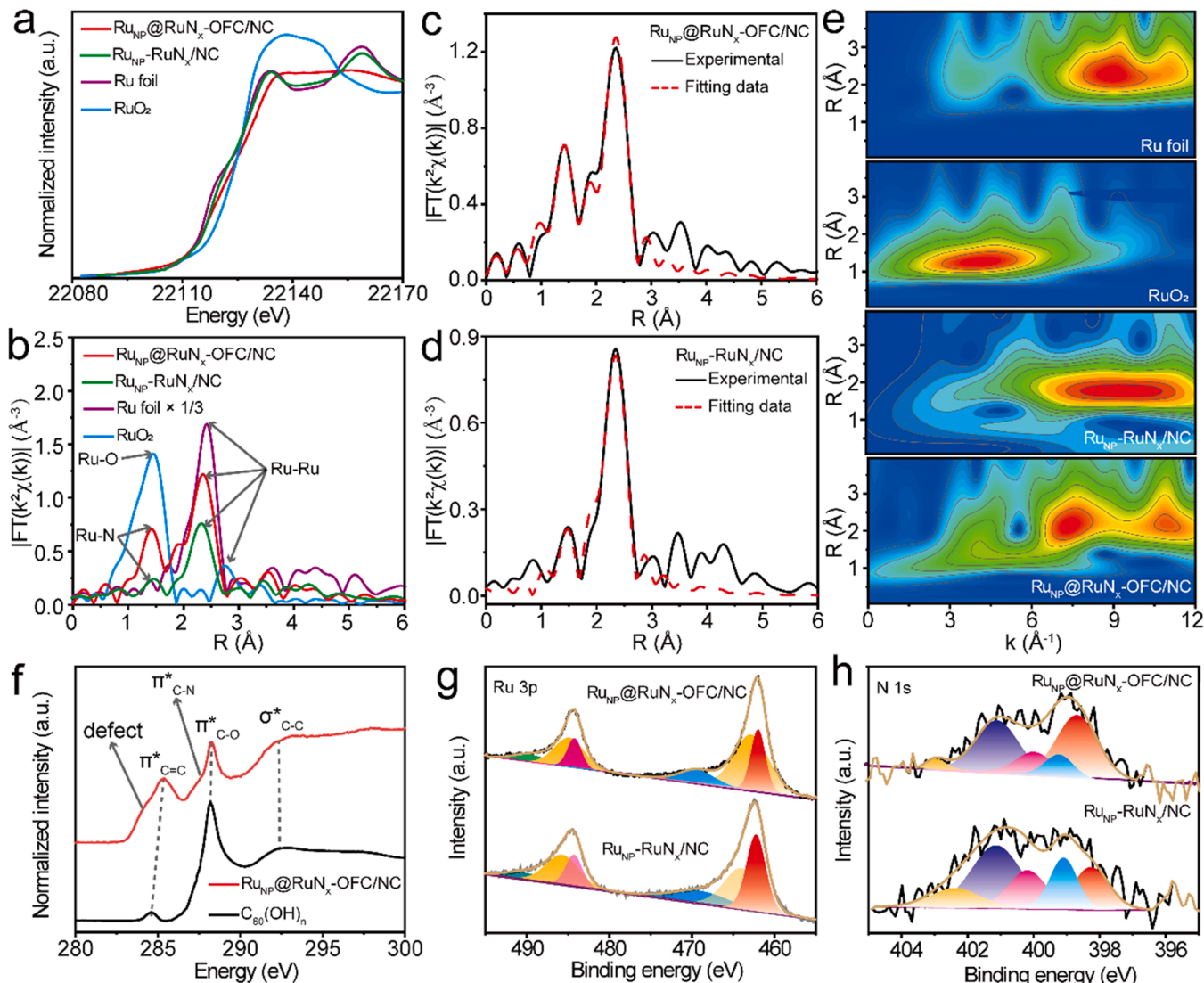


**Fig. 3.** Coordination structure and chemical state of Ru<sub>NP</sub>@Ru<sub>Nx</sub>-OFC/NC. (a) Normalized Ru K-edge XANES spectra and (b) Fourier transform of Ru K-edge EXAFS of Ru<sub>NP</sub>@Ru<sub>Nx</sub>-OFC/NC (red), Ru<sub>NP</sub>-Ru<sub>Nx</sub>/NC (green), Ru foil (purple) and RuO<sub>2</sub> (blue). EXAFS fitting curves in R space of (c) Ru<sub>NP</sub>@Ru<sub>Nx</sub>-OFC/NC and (d) Ru<sub>NP</sub>-Ru<sub>Nx</sub>/NC. (e) Wavelet transform of the Ru K-edge for the EXAFS spectra of Ru<sub>NP</sub>@Ru<sub>Nx</sub>-OFC/NC, Ru<sub>NP</sub>-Ru<sub>Nx</sub>/NC, Ru foil and RuO<sub>2</sub>. (f) Normalized C K-edge XANES spectra of Ru<sub>NP</sub>@Ru<sub>Nx</sub>-OFC/NC and C<sub>60</sub>(OH)<sub>n</sub>. High-resolution XPS spectra of (g) Ru 3p and (h) N 1s for Ru<sub>NP</sub>@Ru<sub>Nx</sub>-OFC/NC and Ru<sub>NP</sub>-Ru<sub>Nx</sub>/NC.

interaction in Ru NP. Besides, a minor peak centered at 1.43 Å was also observed in the spectrum of Ru<sub>NP</sub>@Ru<sub>Nx</sub>-OFC/NC, which could be assigned to the Ru-N scattering path [56]. For comparison, the peak of Ru-N bond in the FT EXAFS curve of Ru<sub>NP</sub>-Ru<sub>Nx</sub>/NC was much weaker and slightly upshifted, due to the low amount of sing-atomic Ru on the planar carbon matrix. Accordingly, EXAFS refinement of Ru<sub>NP</sub>@Ru<sub>Nx</sub>-OFC/NC (Fig. 3c), Ru<sub>NP</sub>-Ru<sub>Nx</sub>/NC (Fig. 3d) and Ru foil (Fig. S14) was then performed and the selected fitting parameters are listed in Table S1. The best-fitting result of Ru<sub>NP</sub>@Ru<sub>Nx</sub>-OFC/NC clearly exhibited two main peaks by using a Ru-Ru and Ru-N shell with a bond length of 2.65 and 1.94 Å, respectively. Moreover, the coordination number (CN) was estimated to be 2.0 for Ru-N and 3.7 for Ru-Ru. The former was smaller than that (12) of Ru foil, probably due to the formation of Ru nanoparticles [7], whereas the latter was abnormally large relative to the particle size observed in the TEM images in Fig. 2d. These results validated the coexistence of Ru nanoparticles and single-atomic Ru<sub>Nx</sub> species in Ru<sub>NP</sub>@Ru<sub>Nx</sub>-OFC/NC. The wavelet transform (WT) of the  $k^3$ -weighted Ru K edge EXAFS counter plots of Ru<sub>NP</sub>@Ru<sub>Nx</sub>-OFC/NC, Ru<sub>NP</sub>-Ru<sub>Nx</sub>/NC, Ru foil and RuO<sub>2</sub> were conducted to further support the conclusion above. As can be seen in Fig. 3e, two

dominant peaks located at 10.9 and 7.4 Å<sup>-1</sup> account for the contribute from Ru-Ru and Ru-N [56], respectively. Besides, the C K-edge XANES spectrum of Ru<sub>NP</sub>@Ru<sub>Nx</sub>-OFC/NC and the pristine C<sub>60</sub>(OH)<sub>n</sub> displayed the characteristic resonance (Fig. 3f). Three obvious peaks located at 284.5, 288.2 and 292.8 eV in C<sub>60</sub>(OH)<sub>n</sub> corresponded to the  $\pi^*_{C=C}$ ,  $\pi^*_{C=O}$  and  $\sigma^*_{C-C}$  [57], respectively. These peaks were upshifted slightly in Ru<sub>NP</sub>@Ru<sub>Nx</sub>-OFC/NC, which may be caused by the electronic interaction of the carbon cage with Ru nanoparticles and Ru single atoms. Particularly, a shoulder peak at 284.1 eV in Ru<sub>NP</sub>@Ru<sub>Nx</sub>-OFC/NC was assigned to structure defect, and the peak appeared at 287.5 eV could be attributed to  $\pi^*_{C-N}$  resonance on the carbon cage and the nitrogen-doped substrate [58].

The electronic structure of Ru<sub>NP</sub>@Ru<sub>Nx</sub>-OFC/NC was further investigated by XPS measurement. The XPS survey spectrum of Ru<sub>NP</sub>@Ru<sub>Nx</sub>-OFC/NC reveals the presence of Ru, N, C and O in the sample (Fig. S15). From the high-resolution of the deconvoluted Ru 3p spectrum displayed in Fig. 3g, the peak for Ru 3p<sub>3/2</sub> spectrum located at 462.0 and 462.9 eV were attributed to Ru<sup>0</sup> and oxidized Ru<sup>x+</sup> species, corresponding to the metallic state in Ru NP and single-atomic state in Ru<sub>Nx</sub> species [41], respectively. While the peaks at 484.2 and 485.0 eV were assigned to the

same species as well and the smaller shoulder at 469.7 and 490.1 eV could be ascribed to the satellite peaks. In contrast, for the  $\text{Ru}_{\text{NP}}\text{-RuN}_x\text{/NC}$  sample, the Ru 3p<sub>3/2</sub> peaks was located at 462.1 and 464.1 eV, where the former was very close to the binding energy of metallic Ru in  $\text{Ru}_{\text{NP}}\text{@RuN}_x\text{-OFC/NC}$ , but the latter extremely deviated from the single-atomic Ru species observed in  $\text{Ru}_{\text{NP}}\text{@RuN}_x\text{-OFC/NC}$ , indicative of different electronic structure of single-atomic Ru in these two samples. Moreover, the high-resolution N 1s spectrum of  $\text{Ru}_{\text{NP}}\text{@RuN}_x\text{-OFC/NC}$  can be fitted into five peaks (Fig. 3h and Table S2), i.e., pyridinic N (398.7 eV), metallic N (399.3 eV), pyrrolic N (400.0 eV), graphitic N (401.1 eV) and oxidized N (402.9 eV) [59]. Meanwhile, the C-N peak at 288.2 and 286.4 eV was clearly recorded in the C 1s spectrum of  $\text{Ru}_{\text{NP}}\text{@RuN}_x\text{-OFC/NC}$  and  $\text{Ru}_{\text{NP}}\text{-RuN}_x\text{/NC}$  (Fig. S15), respectively, conforming the nitrogen doping in the carbon matrix. Therefore, the configuration of  $\text{Ru}_{\text{NP}}\text{@RuN}_x\text{-OFC/NC}$  could be defined as a Ru NP

encapsulated into  $\text{RuN}_x$ -decorated oxyfullerene-like carbon cage anchored on nitrogen-doped carbon matrix, whereas the Ru NP supported on the planar surface of nitrogen-doped carbon substrate decorated with single-atomic Ru was found in  $\text{Ru}_{\text{NP}}\text{-RuN}_x\text{/NC}$ . The present results suggested that the fullerenol molecules play a vital role in regulating the formation of Ru single atom localized on the fullerene-like carbon cage.

### 3.3. HER activity evaluation of $\text{Ru}_{\text{NP}}\text{@RuN}_x\text{-OFC/NC}$

The electrochemical performance of  $\text{Ru}_{\text{NP}}\text{@RuN}_x\text{-OFC/NC}$  for HER was evaluated both in 0.5 M H<sub>2</sub>SO<sub>4</sub> and 1 M KOH aqueous solution using a standard three-electrode system. As reference,  $\text{Ru}_{\text{NP}}\text{-RuN}_x\text{/NC}$ ,  $\text{Ru}_{\text{SA}}\text{/NC}$ ,  $\text{Ru}_{\text{NP}}\text{/NC}$  and the commercial benchmark Pt/C were also examined under the same condition. To be accurate, the reference SCE were

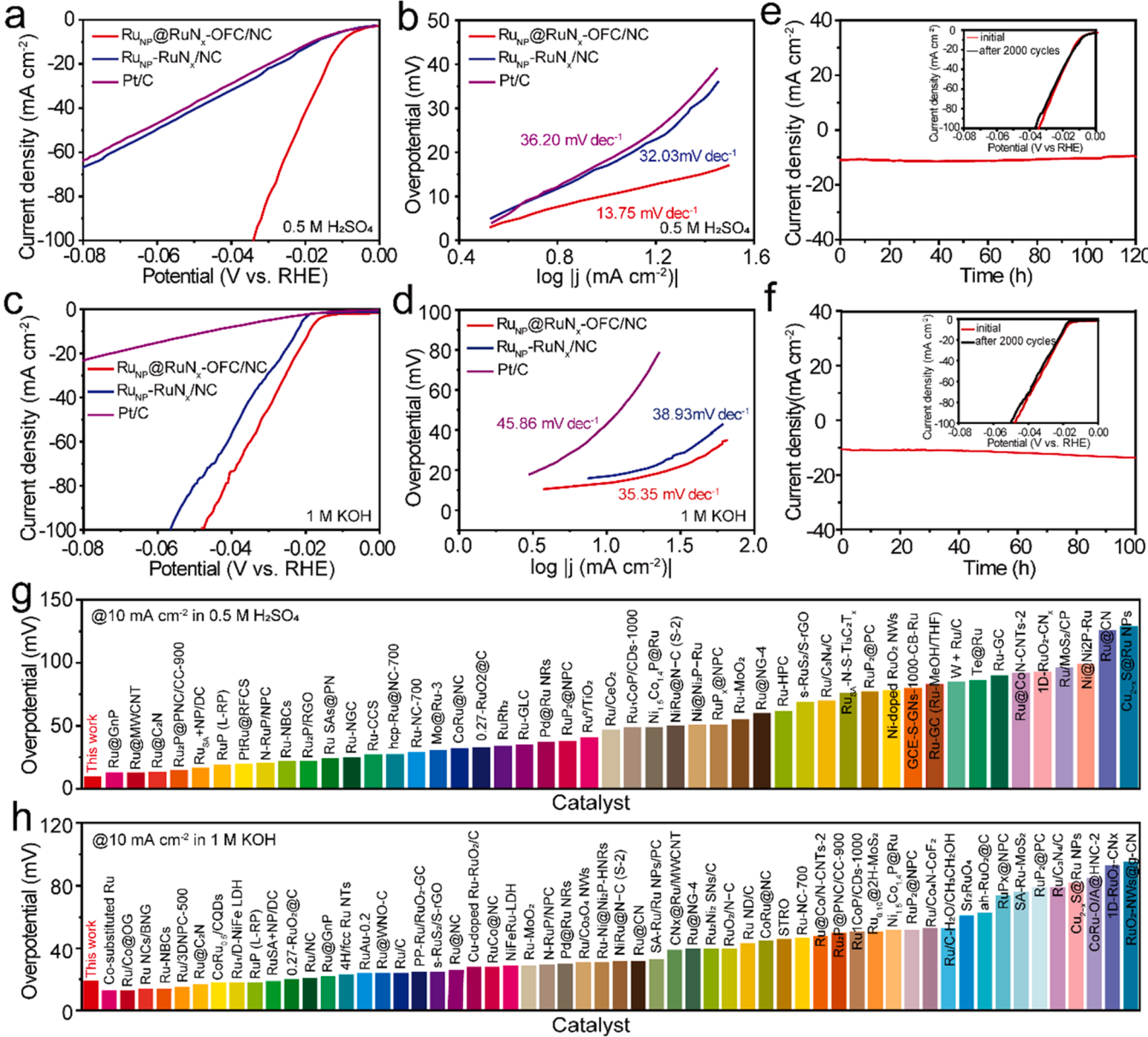


**Fig. 4.** HER activity evaluation of  $\text{Ru}_{\text{NP}}\text{@RuN}_x\text{-OFC/NC}$ . LSV curves of  $\text{Ru}_{\text{NP}}\text{@RuN}_x\text{-OFC/NC}$ ,  $\text{Ru}_{\text{NP}}\text{-RuN}_x\text{/NC}$  and Pt/C in (a) 0.5 M H<sub>2</sub>SO<sub>4</sub> and (c) 1 M KOH. The corresponding Tafel plots of  $\text{Ru}_{\text{NP}}\text{@RuN}_x\text{-OFC/NC}$ ,  $\text{Ru}_{\text{NP}}\text{-RuN}_x\text{/NC}$  and Pt/C in (b) 0.5 M H<sub>2</sub>SO<sub>4</sub> and (d) 1 M KOH. Long-term chronoamperometric test of  $\text{Ru}_{\text{NP}}\text{@RuN}_x\text{-OFC/NC}$  in (e) 0.5 M H<sub>2</sub>SO<sub>4</sub> and (f) 1 M KOH at current density of 10 mA cm<sup>-2</sup>, inset of e and f showing the LSV curves of  $\text{Ru}_{\text{NP}}\text{@RuN}_x\text{-OFC/NC}$  before (red) and after (black) 2000 CV cycles. Comparison of the overpotential at 10 mA cm<sup>-2</sup> ( $\eta_{10}$ ) in (g) 0.5 M H<sub>2</sub>SO<sub>4</sub> and (h) 1 M KOH for  $\text{Ru}_{\text{NP}}\text{@RuN}_x\text{-OFC/NC}$  with recently-reported Ru-based HER electrocatalysts.

calibrated against RHE in H<sub>2</sub>-saturated 0.5 M H<sub>2</sub>SO<sub>4</sub> and 1 M KOH medium before all the test (Fig. S16 and S17) [60]. Fig. 4a and S18 illustrated the LSV curves of Ru<sub>NP</sub>@RuN<sub>x</sub>-OFC/NC, Ru<sub>NP</sub>-RuN<sub>x</sub>/NC, Ru<sub>SA</sub>/NC, Ru<sub>NP</sub>/NC and Pt/C measured in N<sub>2</sub>-saturated 0.5 M H<sub>2</sub>SO<sub>4</sub> with a scan rate of 1 mV s<sup>-1</sup>. Apparently, the Ru<sub>NP</sub>@RuN<sub>x</sub>-OFC/NC possessed a huge superiority with highest current density in the whole potential range. Specifically, Ru<sub>NP</sub>@RuN<sub>x</sub>-OFC/NC presented an ultrasmall overpotential ( $\eta_{10}$ ) of merely 10 mV to deliver a current density of 10 mA cm<sup>-2</sup> (i.e., the critical current density expected for a 12.3% efficient solar water-splitting device) [61,62], much lower than that of Ru<sub>NP</sub>-RuN<sub>x</sub>/NC (17 mV), Ru<sub>SA</sub>/NC (74 mV), Ru<sub>NP</sub>/NC (81 mV) (Fig. S18) and even the commercial Pt/C (19 mV). The reaction kinetics was subsequently analyzed by the corresponding Tafel slope. As displayed in Fig. 4b, the Tafel slope for Ru<sub>NP</sub>@RuN<sub>x</sub>-OFC/NC, Ru<sub>NP</sub>-RuN<sub>x</sub>/NC and Pt/C were 13.75, 32.03 and 36.20 mV dec<sup>-1</sup>, respectively, indicating a faster reaction kinetics of Ru<sub>NP</sub>@RuN<sub>x</sub>-OFC/NC in the electrocatalytic HER process. The small Tafel slope suggests that the rate-limiting step is the recombination of chemical adsorbed hydrogen and the HER over the catalysts follow the Volmer-Tafel mechanism [9,63]. The charge transfer kinetics was then examined by the EIS measurement. The Nyquist plot of Ru<sub>NP</sub>@RuN<sub>x</sub>-OFC/NC (Fig. S19) exhibited a smaller semicircle diameter, revealing a favorable charge transfer resistance ( $R_{ct}$ ) of 16.37 Ω compared with Ru<sub>NP</sub>-RuN<sub>x</sub>/NC (17.42 Ω) and Pt/C (22.53 Ω). The ECSA were further calculated using the double-layer capacitance methods [64]. According to the  $C_{dl}$  value of the catalysts (Fig. S20), the ECSA were estimated to be 54.80 cm<sup>2</sup> for Ru<sub>NP</sub>@RuN<sub>x</sub>-OFC/NC, 18.74 cm<sup>2</sup> for Ru<sub>NP</sub>-RuN<sub>x</sub>/NC and 9.82 cm<sup>2</sup> for Pt/C. The enhanced HER performance of Ru<sub>NP</sub>@RuN<sub>x</sub>-OFC/NC would be due to the faster charge transfer between the active sites and the electrolyte, which can be ascribed to the contribute from the conductive oxyfullerene-like carbon shell.

The HER activity of Ru<sub>NP</sub>@RuN<sub>x</sub>-OFC/NC, Ru<sub>NP</sub>-RuN<sub>x</sub>/NC and Pt/C was further investigated in N<sub>2</sub>-saturated 1 M KOH solution. Interestingly, as depicted in Fig. 4c, Ru<sub>NP</sub>@RuN<sub>x</sub>-OFC/NC and Ru<sub>NP</sub>-RuN<sub>x</sub>/NC displayed comparable HER activity, both superior to commercial Pt/C. Remarkably, to reach a current density of 10 mA cm<sup>-2</sup>, the Ru<sub>NP</sub>@RuN<sub>x</sub>-OFC/NC catalyst required an overpotential of 19 mV, which was superior to Ru<sub>NP</sub>-RuN<sub>x</sub>/NC (23 mV), Ru<sub>SA</sub>/NC (56 mV), Ru<sub>NP</sub>/NC (67 mV) (Fig. S21) and extensively surpassed commercial Pt/C (46 mV). Moreover, the Ru<sub>NP</sub>@RuN<sub>x</sub>-OFC/NC exhibited a smaller Tafel slope of 35.35 mV dec<sup>-1</sup> (Fig. 4d), compared to that of Ru<sub>NP</sub>-RuN<sub>x</sub>/NC (38.93 mV dec<sup>-1</sup>) and Pt/C (45.86 mV dec<sup>-1</sup>), indicating that Ru<sub>NP</sub>@RuN<sub>x</sub>-OFC/NC catalyzed the alkaline HER reaction much faster than Ru<sub>NP</sub>-RuN<sub>x</sub>/NC and Pt/C. The EIS measurement revealed a favorable charge transfer for Ru<sub>NP</sub>@RuN<sub>x</sub>-OFC/NC with a  $R_{ct}$  value of 10.81 Ω (Fig. S22), relative to Ru<sub>NP</sub>-RuN<sub>x</sub>/NC (16.97 Ω) and Pt/C (24.32 Ω). The ECSA of Ru<sub>NP</sub>@RuN<sub>x</sub>-OFC/NC in alkaline solution reflected from the  $C_{dl}$  was determined to be 128.52 cm<sup>2</sup> (Fig. S23), larger than that of Ru<sub>NP</sub>-RuN<sub>x</sub>/NC (17.85 cm<sup>2</sup>) and Pt/C (4.46 cm<sup>2</sup>), implying much more active reaction sites for Ru<sub>NP</sub>@RuN<sub>x</sub>-OFC/NC during the HER process.

The stability of the Ru<sub>NP</sub>@RuN<sub>x</sub>-OFC/NC catalyst was tested both in acidic and basic condition. It can be seen from Fig. 4e and f that after continuous CV scanning for 2000 cycles, the Ru<sub>NP</sub>@RuN<sub>x</sub>-OFC/NC shows a negligible negative shift in 0.5 M H<sub>2</sub>SO<sub>4</sub> and 1 M KOH aqueous solution. The long-term chronoamperometry measurement was then conducted, which demonstrated that the Ru<sub>NP</sub>@RuN<sub>x</sub>-OFC/NC possessed a robust durability for at least 120 h in 0.5 M H<sub>2</sub>SO<sub>4</sub> and 100 h in 1 M KOH. TEM images verified that after the long-term chronoamperometry test the morphology of Ru<sub>NP</sub>@RuN<sub>x</sub>-OFC/NC remained intact (Fig. S24). XPS results signified that after the chronoamperometric measurement the chemical state of Ru do not change, further conforming the robust durability of Ru<sub>NP</sub>@RuN<sub>x</sub>-OFC/NC (Fig. S25).

The overpotential of Ru<sub>NP</sub>@RuN<sub>x</sub>-OFC/NC at the current density of 10 mA cm<sup>-2</sup> in acid (Fig. 4g and Table S3) and alkaline (Fig. 4h and Table S4) was compared with other Ru-based HER electrocatalysts reported recently. The results demonstrated that the present Ru<sub>NP</sub>@RuN<sub>x</sub>-

OFC/NC catalyst outperformed the benchmark Pt/C, and surpassed most of the recently-reported Ru-based HER catalyst both in acidic and basic condition.

To identify the intrinsic active site of the Ru<sub>NP</sub>@RuN<sub>x</sub>-OFC/NC catalyst, KSCN and EDTA were used as poisoning agents to clarify the contribution of Ru NP and single-atomic RuN<sub>x</sub> species. In general, KSCN is able to cover both the nanoparticle and the single atom sites, whereas EDTA forms coordination bond predominantly with the latter [40]. As shown in Fig. S26, when EDTA was added into the acidic electrolyte, the  $\eta_{10}$  value shifted negatively by 9 mV, and the value was 15 mV in the case of KSCN. The different poisoning effect by KSCN and EDTA indicated that both Ru NP and single-atomic RuN<sub>x</sub> species on the carbon shell make a contribute to the enhanced HER activity, where the latter probably play a major role. Meanwhile, the poisoning experiment for Ru<sub>NP</sub>-RuN<sub>x</sub>/NC suggested that the active site was Ru NP for the fact that single-atomic Ru take negligible effect over HER process (Fig. S27). This result manifested that the facile electronic communication between Ru NP and single-atomic RuN<sub>x</sub> species in Ru<sub>NP</sub>@RuN<sub>x</sub>-OFC/NC indeed take effect on boosting the reactive site, and thus improving the electrocatalytic HER activity.

To assess the inherent electrocatalytic efficiency of Ru<sub>NP</sub>@RuN<sub>x</sub>-OFC/NC, the TOF values in 0.5 M H<sub>2</sub>SO<sub>4</sub> and 1 M KOH aqueous condition were calculated based on the estimated number of active sites, which can be obtained by the copper UPD method (Fig. S28) [32]. The obtained TOF value was 0.77 H<sub>2</sub> s<sup>-1</sup> in 0.5 M H<sub>2</sub>SO<sub>4</sub> and 0.49 H<sub>2</sub> s<sup>-1</sup> in 1 M KOH at overpotential of 100 mV, which was comparable with the representative HER catalysts reported recently (Fig. S29, Table S5 and S6). To further evaluate the HER activity of Ru<sub>NP</sub>@RuN<sub>x</sub>-OFC/NC from different perspective, the mass and ECSA-normalized LSV curves were obtained (Fig. S30–33) [65]. Clearly, in both cases, the Ru<sub>NP</sub>@RuN<sub>x</sub>-OFC/NC exhibited a superior activity compared with Ru<sub>NP</sub>-RuN<sub>x</sub>/NC and even the benchmark Pt/C, suggesting that Ru<sub>NP</sub>@RuN<sub>x</sub>-OFC/NC has advantages over Pt/C in terms of the overall HER performance.

#### 3.4. Electrocatalytic performance of Ru<sub>NP</sub>@RuN<sub>x</sub>-OFC/NC at industrial-level current density

For practical use, the hydrogen production performance under industrial-level current output larger than 500 mA cm<sup>-2</sup> was investigated by coating the catalyst powder onto the surface of carbon paper (CP). As shown in Fig. 5a, Ru<sub>NP</sub>@RuN<sub>x</sub>-OFC/NC displayed excellent HER activity in the range of 3000 mA cm<sup>-2</sup> in acidic condition. Specifically, it can reach current density of 500, 1000, 2000 and 3000 mA cm<sup>-2</sup> with overpotential of 174, 259, 352 and 380 mV, respectively, much lower than those (202, 298, 417 and 476 mV) of Ru<sub>NP</sub>-RuN<sub>x</sub>/NC (Fig. 5b), outperforming most of the recently-reported HER electrocatalysts (Fig. 5c and Table S7). Besides, in the alkaline medium Ru<sub>NP</sub>@RuN<sub>x</sub>-OFC/NC also exhibited superior activity (Fig. 5d), e.g., to reach the current density of 500, 1000, 2000 and 3000 mA cm<sup>-2</sup>, it required overpotentials of 92, 153, 252 and 345 mV (Fig. 5b), respectively, which was superior to Ru<sub>NP</sub>-RuN<sub>x</sub>/NC and even surpassed many recently-reported HER electrocatalysts in alkaline medium (Fig. 5e and Table S8). Moreover, after continuous CV scanning for 1000 cycles, the LSV curves of Ru<sub>NP</sub>@RuN<sub>x</sub>-OFC/NC both in acid and alkaline condition showed negligible decay (dashed lines in Fig. 5a and d). Chronoamperometric measurement demonstrated that the electrocatalytic activity of Ru<sub>NP</sub>@RuN<sub>x</sub>-OFC/NC could sustain at least for 10 h under current density of 1000 and 700 mA cm<sup>-2</sup> in 0.5 M H<sub>2</sub>SO<sub>4</sub> and 1 M KOH (Fig. 5f), respectively. Furthermore, a homemade two-electrode overall water splitting system using Ru<sub>NP</sub>@RuN<sub>x</sub>-OFC/NC and the commercial IrO<sub>2</sub> as the cathode and anode, respectively, was built and tested in 1 M KOH (defined as Ru<sub>NP</sub>@RuN<sub>x</sub>-OFC/NC||IrO<sub>2</sub> for clarity). The LSV curves show that the Ru<sub>NP</sub>@RuN<sub>x</sub>-OFC/NC||IrO<sub>2</sub> cell required a cell voltage of 1.337 and 1.615 V to achieve the current density of 10 and 100 mA cm<sup>-2</sup> (Fig. 5g), respectively, outperforming the Pt/C||IrO<sub>2</sub>

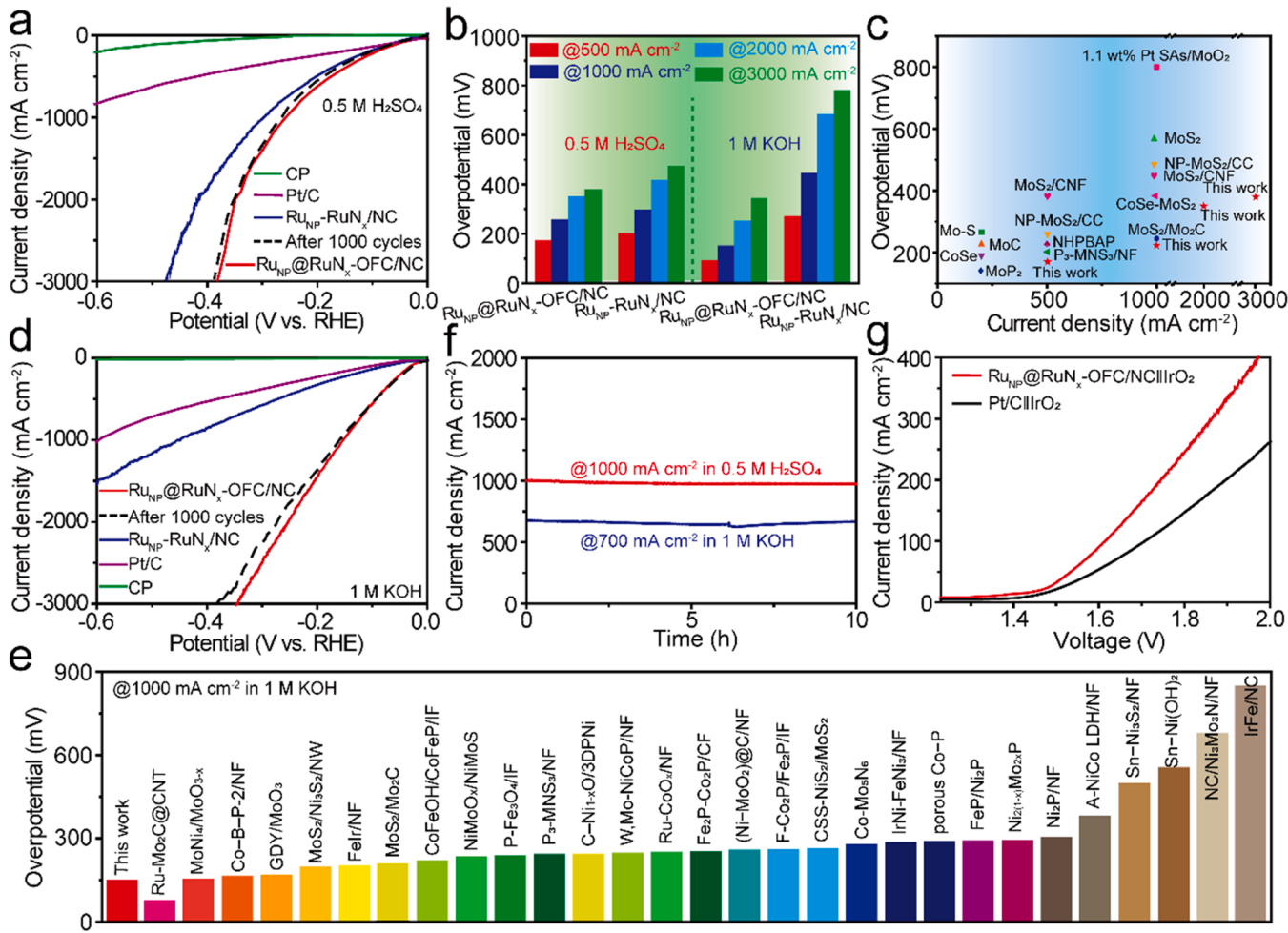


**Fig. 5.** HER and overall water splitting performance at large-current condition. LSV curves of Ru<sub>NP</sub>@RuN<sub>x</sub>-OFC/NC, Ru<sub>NP</sub>-RuN<sub>x</sub>/NC, Pt/C and CP in (a) 0.5 M H<sub>2</sub>SO<sub>4</sub> and (d) 1 M KOH, the dashed lines in a and d refer to the LSV curves of Ru<sub>NP</sub>@RuN<sub>x</sub>-OFC/NC after 1000 CV cycles. (b) Comparison of the overpotentials at current density of 500, 1000, 2000 and 3000 mA cm<sup>-2</sup> for Ru<sub>NP</sub>@RuN<sub>x</sub>-OFC/NC and Ru<sub>NP</sub>-RuN<sub>x</sub>/NC both in 0.5 M H<sub>2</sub>SO<sub>4</sub> (left panel) and 1 M KOH (right panel). (c) Comparison of the overpotential at 500, 1000, 2000 and 3000 mA cm<sup>-2</sup> of Ru<sub>NP</sub>@RuN<sub>x</sub>-OFC/NC in 0.5 M H<sub>2</sub>SO<sub>4</sub> with other recently-reported HER electrocatalysts. (e) Comparison of the overpotential at 1000 mA cm<sup>-2</sup> of Ru<sub>NP</sub>@RuN<sub>x</sub>-OFC/NC in 1 M KOH with other recently-reported HER electrocatalysts. (f) Long-term chronoamperometric test of Ru<sub>NP</sub>@RuN<sub>x</sub>-OFC/NC in 0.5 M H<sub>2</sub>SO<sub>4</sub> (red) and 1 M KOH (blue) at current density of 1000 and 700 mA cm<sup>-2</sup>, respectively. (g) LSV curves of Ru<sub>NP</sub>@RuN<sub>x</sub>-OFC/NC||IrO<sub>2</sub> and Pt/C||IrO<sub>2</sub> electrolytic cell measured in 1 M KOH.

counterpart (1.437 and 1.708 V), and comparable to many other reported electrocatalysts (Table S9). Besides, the Ru<sub>NP</sub>@RuN<sub>x</sub>-OFC/NC||IrO<sub>2</sub> cell exhibited desirable catalytic durability. As displayed in Fig. S34, the current density exhibited negligible decay after continuously operating for 50 h. Overall, considering the high activity and favorable durability, Ru<sub>NP</sub>@RuN<sub>x</sub>-OFC/NC would be a promising alternative HER catalyst to Pt/C for practical water splitting.

### 3.5. Theoretical investigation on the HER mechanism of Ru<sub>NP</sub>@RuN<sub>x</sub>-OFC/NC

DFT calculation was further performed to investigate the electrocatalytic mechanism behind the HER process. The Sabatier principle suggests that  $\Delta G_{H^*}$  is a principle descriptor of HER activity. For a super HER electrocatalyst, the  $\Delta G_{H^*}$  value close to zero is desirable for the H<sup>\*</sup> adsorption and desorption [8,66]. Therefore, the optimized structure for each intermediate on the catalysts of Ru<sub>NP</sub>@RuN<sub>4</sub>-FC and Ru<sub>NP</sub>-RuN<sub>4</sub>/PC were first constructed (Fig. S35) and the energy barrier for each reaction step were calculated in acidic and alkaline medium (Fig. 6a and b). For comparison, another control models of Ru<sub>SA</sub>/PC and Ru<sub>NP</sub>/PC were also constructed (Fig. S35). As shown in Fig. 6a, in acidic condition, the  $\Delta G_{H^*}$  was calculated to be  $-0.02$  eV in the case of

Ru<sub>NP</sub>@RuN<sub>4</sub>-FC, much lower than that ( $-0.22$  eV) of Ru<sub>NP</sub>-RuN<sub>4</sub>/PC, indicative of a more favorable HER activity for Ru<sub>NP</sub>@RuN<sub>4</sub>-FC in acidic condition. While in basic medium, considering the large energy barrier of water dissociation process,  $\Delta G_{H^*}$  alone is unable to describe the apparent HER activity [58]. As displayed in Fig. 6b, although the  $\Delta G_{H^*}$  of Ru<sub>NP</sub>@RuN<sub>4</sub>-FC (0.79 eV) is a little larger than that of Ru<sub>NP</sub>-RuN<sub>4</sub>/PC (0.59 eV), the significant free energy of water dissociation on Ru<sub>NP</sub>-RuN<sub>4</sub>/PC ( $-0.87$  eV) compared with Ru<sub>NP</sub>@RuN<sub>4</sub>-FC (0.02 eV) extremely retards the formation of adsorbed H<sup>\*</sup> and OH<sup>\*</sup>. Obviously, the step for the departure of OH<sup>\*</sup> exhibited the largest energy barrier in the whole HER process for Ru<sub>NP</sub>@RuN<sub>4</sub>-FC and Ru<sub>NP</sub>-RuN<sub>4</sub>/PC, indicating it is the rate-determining step (RDS) [67]. For Ru<sub>NP</sub>-RuN<sub>4</sub>/PC, the energy barrier of RDS is 1.47 eV. This value is remarkably reduced to 0.76 eV in Ru<sub>NP</sub>@RuN<sub>4</sub>-FC. Notably, the lower water dissociation barrier of Ru<sub>NP</sub>@RuN<sub>4</sub>-FC is associated with the kinetic transitional state (TS). It can be seen that the kinetic water dissociation on Ru<sub>NP</sub>@RuN<sub>4</sub>-FC via a TS intermediate was found to be exothermic with a barrier of 0.28 eV, smaller than that (0.30 eV) on Ru<sub>NP</sub>-RuN<sub>4</sub>/PC. Therefore, it is clear that Ru<sub>NP</sub>@RuN<sub>4</sub>-FC exhibit superior reaction activity toward HER in alkaline condition both from the thermodynamic viewpoint and kinetic transition-state theory. By the way, it is noted that even the free energy of water dissociation for Ru<sub>NP</sub>@RuN<sub>4</sub>-FC seems

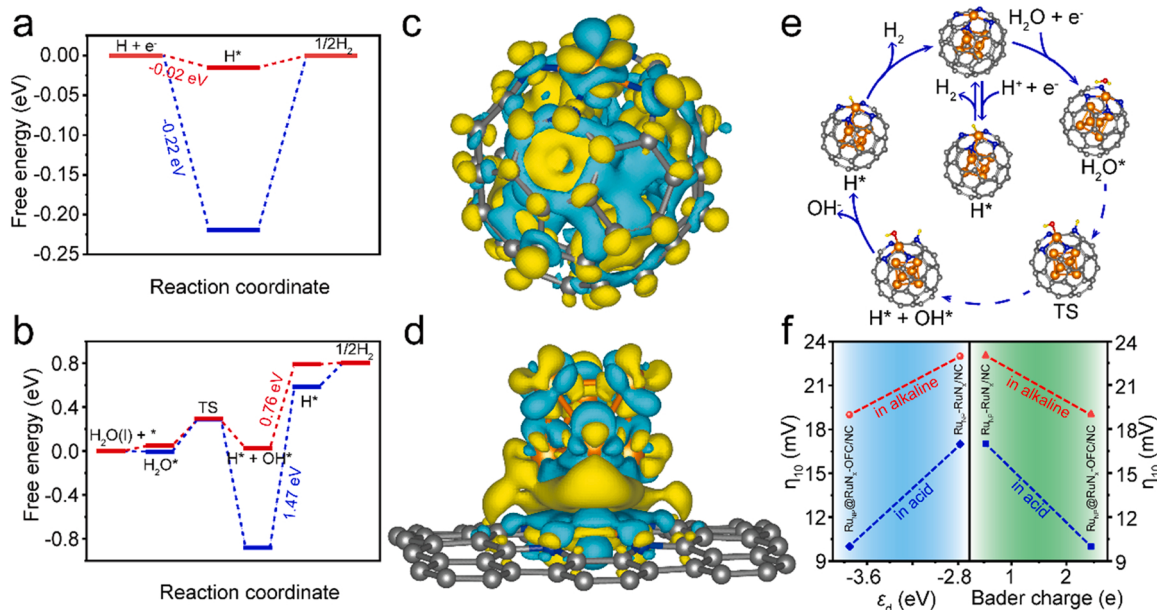


**Fig. 6.** DFT calculation on the reaction free energy and electronic structure. Free energy diagram for HER in (a) acid and (b) alkaline condition on  $\text{Ru}_{\text{NP}}@\text{RuN}_4\text{-FC}$  (red curve) and  $\text{Ru}_{\text{NP}}\text{-RuN}_4/\text{PC}$  (blue curve). Charge density difference plot of (c)  $\text{Ru}_{\text{NP}}@\text{RuN}_4\text{-FC}$  and (d)  $\text{Ru}_{\text{NP}}\text{-RuN}_4/\text{PC}$ . Yellow and light green contours represent the electron accumulation and deletion, respectively. The balls in gold, blue and gray represent Ru, N and C atoms, respectively. (e) Proposed possible HER mechanism for  $\text{Ru}_{\text{NP}}@\text{RuN}_4\text{-FC}$  in acid and alkaline medium. (f) Linear relationship of  $\eta_{10}$  for HER over  $\text{Ru}_{\text{NP}}@\text{RuN}_4\text{-FC}$  and  $\text{Ru}_{\text{NP}}\text{-RuN}_4/\text{PC}$  in acid (blue) and alkaline (red) condition against  $\epsilon_d$  (left panel) and Bader charge (right panel).

inferior to  $\text{Ru}_{\text{NP}}/\text{PC}$  ( $-0.96$  eV), however, the larger kinetic barrier of TS in the latter case retards the whole electrocatalytic reaction process (Fig. S36). Therefore, in the core-shell structure of  $\text{Ru}_{\text{NP}}@\text{RuN}_4\text{-FC}$ , the spatial geometric structure plays a critical role in regulating the electronic interplay between the single-atomic Ru and Ru NP, and thus reducing the free energy of hydrogen production.

The differential charge density distribution diagrams of  $\text{Ru}_{\text{NP}}@\text{RuN}_4\text{-FC}$  and  $\text{Ru}_{\text{NP}}\text{-RuN}_4/\text{PC}$  are then calculated to further investigate the electronic characteristics. Apparently as depicted in Fig. 6c and d, for  $\text{Ru}_{\text{NP}}@\text{RuN}_4\text{-FC}$  the electrons mainly accumulate on the  $\pi$ -conjugated carbon cage and especially focus on the single-atomic  $\text{RuN}_4$  moiety. Such electron-sufficient atomic Ru site in  $\text{Ru}_{\text{NP}}@\text{RuN}_4\text{-FC}$  would facilitate the adsorption of water, lowering the energy barrier of RDS process [8]. While in  $\text{Ru}_{\text{NP}}\text{-RuN}_4/\text{PC}$ ,  $\text{H}_2\text{O}$  molecules prefer to attack Ru NP instead of  $\text{RuN}_4$  site owing to the steric hindrance of the Ru NP (Fig. S35). Therefore, the transferred electrons from Ru NP to  $\text{RuN}_4$  site in  $\text{Ru}_{\text{NP}}\text{-RuN}_4/\text{PC}$  inevitably reduce the charge density on Ru NP and prohibit the adsorption of  $\text{H}_2\text{O}$  on Ru NP, leading to larger  $\Delta G_{\text{H}^*}$  and  $E_a$ . This result is in good agreement with the free energy diagram of the reaction shown in Fig. 6a and b. Based on the above mechanism analysis, a possible reaction route of HER on  $\text{Ru}_{\text{NP}}@\text{RuN}_4\text{-FC}$  was proposed, as shown in Fig. 6e. Moreover, Bader charge analysis disclosed that the Ru NP inside the carbon cage denotes 2.45 electrons to the Ru single atom in  $\text{Ru}_{\text{NP}}@\text{RuN}_4\text{-FC}$ , whereas only 0.53 electrons was transferred from Ru NP to Ru single atom in  $\text{Ru}_{\text{NP}}\text{-RuN}_4/\text{PC}$ . Considering the charge transfer process is closely associated with the  $d$ -band center, which correlate with the free energy of hydrogen adsorption [41], we found that the Bader charge and  $\epsilon_d$  exhibited a linear relationship toward the HER activity (i.e.  $\eta_{10}$ ) both in acid and alkaline condition as displayed in Fig. 6f. The lower  $\epsilon_d$  and larger Bader charge give rise to smaller overpotential for HER. The above results demonstrated that the electronic communication between the Ru NP inside the fullerene-like carbon cage and the single-atomic Ru on the cage in the case of  $\text{Ru}_{\text{NP}}@\text{RuN}_4\text{-FC}$  indeed make a contribute to the enhanced HER activity.

#### 4. Conclusion

In summary, we synthesized a novel, stable and highly-efficient electrocatalyst for hydrogen production, which composed of a Ru NP core and single-atomic Ru decorated fullerene-like carbon shell supported on nitrogen-doped carbon substrate. The as-obtained  $\text{Ru}_{\text{NP}}@\text{RuN}_x\text{-OFC/NC}$  exhibited an excellent HER activity both in acid and alkaline medium. To reach a current density of  $10 \text{ mA cm}^{-2}$ , the  $\text{Ru}_{\text{NP}}@\text{RuN}_x\text{-OFC/NC}$  required an overpotential of 10 and 19 mV in  $0.5 \text{ M H}_2\text{SO}_4$  and  $1 \text{ M KOH}$ , respectively, outperforming the state-of-the-art Pt/C. Even at industrial-level current output, the newly-synthesized  $\text{Ru}_{\text{NP}}@\text{RuN}_x\text{-OFC/NC}$  could deliver a current density of  $3000 \text{ mA cm}^{-2}$  at overpotential of 380 and 345 mV in acidic and alkaline condition. Experimental and DFT calculation results demonstrated that the electronic transfer from the Ru NP inside the fullerene-like carbon cage to the single-atomic Ru on the cage of  $\text{Ru}_{\text{NP}}@\text{RuN}_x\text{-OFC/NC}$  modulate the charge distribution of the active single-atomic Ru site, thus facilitate the adsorption of water molecules, resulting in the favorable reaction free energy and improved electrocatalytic activity in the HER process. The present work provide a new platform for designing and steering the electronic structures of electrocatalyst in the realm of energy conversion and storage.

#### CRediT authorship contribution statement

**Yongqiang Feng:** Conceptualization, Writing – original draft, Writing – review & editing. **Weihang Feng:** Investigation, Data curation. **Jing Wan:** Data curation. **Junsheng Chen:** Investigation, Data curation. **Hai Wang:** Data curation. **Shumu Li:** Formal analysis. **Tianmi Luo:** Investigation, Data curation. **Yuzhu Hu:** Investigation, Data curation. **Chengke Yuan:** Investigation, Data curation. **Liyun Cao:** Writing – review & editing. **Liangliang Feng:** Writing – review & editing. **Jie Li:** Validation. **Rui Wen:** Validation. **Jianfeng Huang:** Supervision.

## Declaration of Competing Interest

The authors declare that they have no known competing financial interests or personal relationships that could have appeared to influence the work reported in this paper.

## Acknowledgments

This work was financially supported by the National Natural Science Foundation of China (52072226, 52073166), Scientific Research Program Funded by Shaanxi Provincial Education Department (No. 20JY001), the Xi'an Key Laboratory of Green Manufacture of Ceramic Materials Foundation (No. 2019220214SYS017CG039), the Key Program for International S&T Cooperation Projects of Shaanxi Province (2020KW-038, 2020GHJD-04), Science and Technology Program of Xi'an, China (2020KJRC0009) and Science and Technology Resource Sharing Platform of Shaanxi Province (2020PT-022), Science and Technology Plan of Weiyang District, Xi'an (202009). Dr. Y. Q. Feng was grateful for the support from the Science and Technology Youth Stars Project of Shaanxi Province (2021KJXX-35).

## Appendix A. Supporting information

Supplementary data associated with this article can be found in the online version at [doi:10.1016/j.apcatb.2022.121193](https://doi.org/10.1016/j.apcatb.2022.121193).

## References

- [1] J. Wang, F. Xu, H. Jin, Y. Chen, Y. Wang, Non-noble metal-based carbon composites in hydrogen evolution reaction: fundamentals to applications, *Adv. Mater.* 29 (2017), 1605838.
- [2] S. Zhu, X. Qin, F. Xiao, S. Yang, Y. Xu, Z. Tan, J. Li, J. Yan, Q. Chen, M. Chen, M. Shao, The role of ruthenium in improving the kinetics of hydrogen oxidation and evolution reactions of platinum, *Nat. Catal.* 4 (2021) 711–718.
- [3] J.N. Tiwari, S. Sultan, C.W. Myung, T. Yoon, N. Li, M. Ha, A.M. Harzandi, H. J. Park, D.Y. Kim, S.S. Chandrasekaran, W.G. Lee, V. Vij, H. Kang, T.J. Shin, H. S. Shin, G. Lee, Z. Lee, K.S. Kim, Multicomponent electrocatalyst with ultralow Pt loading and high hydrogen evolution activity, *Nat. Energy* 3 (2018) 773–782.
- [4] Y. Feng, X. Wang, J. Huang, P. Dong, J. Ji, J. Li, L. Cao, L. Feng, P. Jin, C. Wang, Decorating CoNi layered double hydroxides nanosheet arrays with fullerene quantum dot anchored on Ni foam for efficient electrocatalytic water splitting and urea electrolysis, *Chem. Eng. J.* 390 (2020), 124525.
- [5] W.-J. Jiang, T. Tang, Y. Zhang, J.-S. Hu, Synergistic modulation of non-precious-metal electrocatalysts for advanced water splitting, *Acc. Chem. Res.* 53 (2020) 1111–1123.
- [6] X. Wu, Z. Wang, D. Zhang, Y. Qin, M. Wang, Y. Han, T. Zhan, B. Yang, S. Li, J. Lai, L. Wang, Solvent-free microwave synthesis of ultra-small Ru-Mo<sub>2</sub>C@CNT with strong metal-support interaction for industrial hydrogen evolution, *Nat. Commun.* 12 (2021) 4018.
- [7] B. Lu, L. Guo, F. Wu, Y. Peng, J.E. Lu, T.J. Smart, N. Wang, Y.Z. Finfrock, D. Morris, P. Zhang, N. Li, P. Gao, Y. Ping, S. Chen, Ruthenium atomically dispersed in carbon outperforms platinum toward hydrogen evolution in alkaline media, *Nat. Commun.* 10 (2019) 631.
- [8] Y. Pan, K. Sun, S. Liu, X. Cao, K. Wu, W.-C. Cheong, Z. Chen, Y. Wang, Y. Li, Y. Liu, D. Wang, Q. Peng, C. Chen, Y. Li, Core-shell ZIF-8@ZIF-67-derived CoP nanoparticle-embedded N-doped carbon nanotube hollow polyhedron for efficient overall water splitting, *J. Am. Chem. Soc.* 140 (2018) 2610–2618.
- [9] Y. Chen, R. Ding, J. Li, J. Liu, Highly active atomically dispersed platinum-based electrocatalyst for hydrogen evolution reaction achieved by defect anchoring strategy, *Appl. Catal. B-Environ.* 301 (2022), 120830.
- [10] Y.H. Li, P.F. Liu, L.F. Pan, H.F. Wang, Z.Z. Yang, L.R. Zheng, P. Hu, H.J. Zhao, L. Gu, H.G. Yang, Local atomic structure modulations activate metal oxide as electrocatalyst for hydrogen evolution in acidic water, *Nat. Commun.* 6 (2015) 8064.
- [11] Y. Zhu, Q. Lin, Y. Zhong, H.A. Tahini, Z. Shao, H. Wang, Metal oxide-based materials as an emerging family of hydrogen evolution electrocatalysts, *Energy Environ. Sci.* 13 (2020) 3361–3392.
- [12] L. Yu, Q. Zhu, S. Song, B. McElhenny, D. Wang, C. Wu, Z. Qin, J. Bao, Y. Yu, S. Chen, Z. Ren, Non-noble metal-nitride based electrocatalysts for high-performance alkaline seawater electrolysis, *Nat. Commun.* 10 (2019) 5106.
- [13] T.L.L. Doan, D.C. Nguyen, S. Prabhakaran, D.H. Kim, D.T. Tran, N.H. Kim, J.H. Lee, Single-atom Co-decorated MoS<sub>2</sub> nanosheets assembled on metal nitride nanorod arrays as an efficient bifunctional electrocatalyst for pH-universal water splitting, *Adv. Funct. Mater.* 31 (2021), 2100233.
- [14] Q. Gao, W. Zhang, Z. Shi, L. Yang, Y. Tang, Structural design and electronic modulation of transition-metal-carbide electrocatalysts toward efficient hydrogen evolution, *Adv. Mater.* 31 (2019), 1802880.
- [15] Q. Jin, B. Ren, H. Cui, C. Wang, Nitrogen and cobalt co-doped carbon nanotube films as binder-free trifunctional electrode for flexible zinc-air battery and self-powered overall water splitting, *Appl. Catal. B-Environ.* 283 (2021), 119643.
- [16] M.A.R. Anjum, M.H. Lee, J.S. Lee, Boron- and nitrogen-codoped molybdenum carbide nanoparticles imbedded in a BCN network as a bifunctional electrocatalyst for hydrogen and oxygen evolution reactions, *ACS Catal.* 8 (2018) 8296–8305.
- [17] Y. Guo, T. Park, J.W. Yi, J. Henzie, J. Kim, Z. Wang, B. Jiang, Y. Bando, Y. Sugahara, J. Tang, Y. Yamauchi, Nanoarchitectonics for transition-metal-sulfide-based electrocatalysts for water splitting, *Adv. Mater.* 31 (2019), 1807134.
- [18] M. Wang, L. Zhang, Y. He, H. Zhu, Recent advances in transition-metal-sulfide-based bifunctional electrocatalysts for overall water splitting, *J. Mater. Chem. A* 9 (2021) 5320–5363.
- [19] C. Huang, L. Yu, W. Zhang, Q. Xiao, J. Zhou, Y. Zhang, P. An, J. Zhang, Y. Yu, N-doped Ni-Mo based sulfides for high-efficiency and stable hydrogen evolution reaction, *Appl. Catal. B-Environ.* 276 (2020), 119137.
- [20] Z. Zhao, D.E. Schipper, A.P. Leitner, H. Thirumalai, J.-H. Chen, L. Xie, F. Qin, M. K. Alam, L.C. Grabow, S. Chen, D. Wang, Z. Ren, Z. Wang, K.H. Whitmire, J. Bao, Bifunctional metal phosphide FeMnP films from single source metal organic chemical vapor deposition for efficient overall water splitting, *Nano Energy* 39 (2017) 444–453.
- [21] P. Xiao, W. Chen, X. Wang, A review of phosphide-based materials for electrocatalytic hydrogen evolution, *Adv. Energy Mater.* 5 (2015), 1500985.
- [22] R. Ge, J. Huo, T. Liao, Y. Liu, M. Zhu, Y. Li, J. Zhang, W. Li, Hierarchical molybdenum phosphide coupled with carbon as a whole pH-range electrocatalyst for hydrogen evolution reaction, *Appl. Catal. B-Environ.* 260 (2020), 118196.
- [23] H. Song, M. Wu, Z. Tang, J.S. Tse, B. Yang, S. Lu, Single atom ruthenium-doped CoP/CDs nanosheets via splicing of carbon-dots for robust hydrogen production, *Angew. Chem. Int. Ed.* 60 (2021) 7234–7244.
- [24] J.-S. Li, M.-J. Huang, Y.-W. Zhou, X.-N. Chen, S. Yang, J.-Y. Zhu, G.-D. Liu, L.-J. Ma, S.-H. Cai, J.-Y. Han, RuP<sub>2</sub>-based hybrids derived from MOFs: highly efficient pH-universal electrocatalysts for the hydrogen evolution reaction, *J. Mater. Chem. A* 9 (2021) 12276–12282.
- [25] Q. Sun, N. Wang, R. Bai, Y. Hui, T. Zhang, D.A. Do, P. Zhang, L. Song, S. Miao, J. Yu, Synergistic effect of ultrasmall metal clusters and zeolites promoting hydrogen generation, *Adv. Sci.* 6 (2019), 1802350.
- [26] P. Jiang, H. Huang, J. Diao, S. Gong, S. Chen, J. Lu, C. Wang, Z. Sun, G. Xia, K. Yang, Y. Yang, L. Wei, Q. Chen, Improving electrocatalytic activity of iridium for hydrogen evolution at high current densities above 1000 mA cm<sup>-2</sup>, *Appl. Catal. B-Environ.* 258 (2019), 117965.
- [27] J. Mahmood, M.A.R. Anjum, S.-H. Shin, I. Ahmad, H.-J. Noh, S.-J. Kim, H.Y. Jeong, J.S. Lee, J.-B. Baek, Encapsulating iridium nanoparticles inside a 3D cage-like organic network as an efficient and durable catalyst for the hydrogen evolution reaction, *Adv. Mater.* 30 (2018), 1805606.
- [28] L. Zhu, H. Lin, Y. Li, F. Liao, Y. Lifshitz, M. Sheng, S.-T. Lee, M. Shao, A rhodium/silicon co-electrocatalyst design concept to surpass platinum hydrogen evolution activity at high overpotentials, *Nat. Commun.* 7 (2016) 12272.
- [29] Q. Wu, M. Luo, J. Han, W. Peng, Y. Zhao, D. Chen, M. Peng, J. Liu, F.M.F. de Groot, Y. Tan, Identifying electrocatalytic sites of the nanoporous copper–ruthenium alloy for hydrogen evolution reaction in alkaline electrolyte, *ACS Energy Lett.* 5 (2020) 192–199.
- [30] S. Zhang, Y. Rui, X. Zhang, R. Sa, F. Zhou, R. Wang, X. Li, Ultrafine cobalt-ruthenium alloy nanoparticles induced by confinement effect for upgrading hydrogen evolution reaction in all-pH range, *Chem. Eng. J.* 417 (2021), 128047.
- [31] W. Li, Y. Zhao, Y. Liu, M. Sun, G.I.N. Waterhouse, B. Huang, K. Zhang, T. Zhang, S. Lu, Exploiting Ru-induced lattice strain in CoRu nanoalloys for robust bifunctional hydrogen production, *Angew. Chem. Int. Ed.* 60 (2021) 3290–3298.
- [32] J. Mahmood, F. Li, S.-M. Jung, M.S. Okyay, I. Ahmad, S.-J. Kim, N. Park, H. Y. Jeong, J.-B. Baek, An efficient and pH-universal ruthenium-based catalyst for the hydrogen evolution reaction, *Nat. Nanotechnol.* 12 (2017) 441–446.
- [33] D.H. Kweon, M.S. Okyay, S.-J. Kim, J.-P. Jeon, H.-J. Noh, N. Park, J. Mahmood, J.-B. Baek, Ruthenium anchored on carbon nanotube electrocatalyst for hydrogen production with enhanced faradaic efficiency, *Nat. Commun.* 11 (2020) 1278.
- [34] J. Ge, D. Zhang, Y. Qin, T. Dou, M. Jiang, F. Zhang, X. Lei, Dual-metallic single Ru and Ni atoms decoration of MoS<sub>2</sub> for high-efficiency hydrogen production, *Appl. Catal. B-Environ.* 298 (2021), 120557.
- [35] K. Liu, X. Zhao, G. Ren, T. Yang, Y. Ren, A.F. Lee, Y. Su, X. Pan, J. Zhang, Z. Chen, J. Yang, X. Liu, T. Zhou, W. Xi, J. Luo, C. Zeng, H. Matsumoto, W. Liu, Q. Jiang, K. Wilson, A. Wang, B. Qiao, W. Li, T. Zhang, Strong metal-support interaction promoted scalable production of thermally stable single-atom catalysts, *Nat. Commun.* 11 (2020) 1263.
- [36] M. Xiao, L. Gao, Y. Wang, X. Wang, J. Zhu, Z. Jin, C. Liu, H. Chen, G. Li, J. Ge, Q. He, Z. Wu, Z. Chen, W. Xing, Ru single-atom site for efficient and durable oxygen reduction catalysis, *J. Am. Chem. Soc.* 141 (2019) 19800–19806.
- [37] Y. Yao, S. Hu, W. Chen, Z.-Q. Huang, W. Wei, T. Yao, R. Liu, K. Zang, X. Wang, G. Wu, W. Yuan, T. Yuan, B. Zhu, W. Liu, Z. Li, D. He, Z. Xue, Y. Wang, X. Zheng, J. Dong, C.-R. Chang, Y. Chen, X. Hong, J. Luo, S. Wei, W.-X. Li, P. Strasser, Y. Wu, Y. Li, Engineering the electronic structure of single atom Ru sites via compressive strain boosts acidic water oxidation electrocatalysis, *Nat. Catal.* 2 (2019) 304–313.
- [38] H. Huang, K. Shen, F. Chen, Y. Li, Metal–organic frameworks as a good platform for the fabrication of single-atom catalysts, *ACS Catal.* 10 (2020) 6579–6586.
- [39] L. Zhang, H. Jang, Y. Wang, Z. Li, W. Zhang, M.G. Kim, D. Yang, S. Liu, X. Liu, J. Cho, Exploring the dominant role of atomic- and nano-ruthenium as active sites for hydrogen evolution reaction in both acidic and alkaline media, *Adv. Sci.* 8 (2021), 2004516.

[40] D. Cao, J. Wang, H. Xu, D. Cheng, Construction of dual-site atomically dispersed electrocatalysts with Ru-C<sub>5</sub> single atoms and Ru-O<sub>4</sub> nanoclusters for accelerated alkali hydrogen evolution, *Small* 17 (2021), 2101163.

[41] P. Su, W. Pei, X. Wang, Y. Ma, Q. Jiang, J. Liang, S. Zhou, J. Zhao, J. Liu, G.Q. Lu, Exceptional electrochemical HER performance with enhanced electron transfer between Ru nanoparticles and single atoms dispersed on a carbon substrate, *Angew. Chem. Int. Ed.* 60 (2021) 16044–16050.

[42] J.N. Tiwari, A.M. Harzandi, M. Ha, S. Sultan, C.W. Myung, H.J. Park, D.Y. Kim, P. Thangavel, A.N. Singh, P. Sharma, S.S. Chandrasekaran, F. Salehnia, J.-W. Jang, H.S. Shin, Z. Lee, K.S. Kim, High-performance hydrogen evolution by Ru single atoms and nitrided-Ru nanoparticles implanted on N-doped graphitic sheet, *Adv. Energy Mater.* 9 (2019), 1900931.

[43] Z. Liu, L. Zeng, J. Yu, L. Yang, J. Zhang, X. Zhang, F. Han, L. Zhao, X. Li, H. Liu, W. Zhou, Charge redistribution of Ru nanoclusters on Co<sub>3</sub>O<sub>4</sub> porous nanowire via the oxygen regulation for enhanced hydrogen evolution reaction, *Nano Energy* 85 (2021), 105940.

[44] Y. Wang, R. Morales-Martínez, X. Zhang, W. Yang, Y. Wang, A. Rodríguez-Fortea, J.M. Poblet, L. Feng, S. Wang, N. Chen, Unique four-electron metal-to-cage charge transfer of th to a C<sub>60</sub> fullerene cage: complete structural characterization of Th@C<sub>3</sub>(8)-C<sub>60</sub>, *J. Am. Chem. Soc.* 139 (2017) 5110–5116.

[45] K. Kokubo, S. Shirakawa, N. Kobayashi, H. Aoshima, T. Oshima, Facile and scalable synthesis of a highly hydroxylated water-soluble fullerol as a single nanoparticle, *Nano Res.* 4 (2011) 204–215.

[46] C. Wei, R.R. Rao, J. Peng, B. Huang, I.E.L. Stephens, M. Risch, Z.J. Xu, Y. Shao-Horn, Recommended practices and benchmark activity for hydrogen and oxygen electrocatalysis in water splitting and fuel cells, *Adv. Mater.* 31 (2019), 1806296.

[47] Y. Feng, R. Wang, P. Dong, X. Wang, W. Feng, J. Chen, L. Cao, L. Feng, C. He, J. Huang, Enhanced electrocatalytic activity of nickel cobalt phosphide nanoparticles anchored on porous N-doped fullerene nanorod for efficient overall water splitting, *ACS Appl. Mater. Interfaces* 13 (2021) 48949–48961.

[48] J.P. Perdew, K. Burke, M. Ernzerhof, Generalized gradient approximation made simple, *Phys. Rev. Lett.* 77 (1996) 3865–3868.

[49] B. Hammer, L.B. Hansen, J.K. Nørskov, Improved adsorption energetics within density-functional theory using revised Perdew-Burke-Ernzerhof functionals, *Phys. Rev. B* 59 (1999) 7413–7421.

[50] P.E. Blöchl, Projector augmented-wave method, *Phys. Rev. B* 50 (1994) 17953–17979.

[51] G. Kresse, D. Joubert, From ultrasoft pseudopotentials to the projector augmented-wave method, *Phys. Rev. B* 59 (1999) 1758–1775.

[52] H.J. Monkhorst, J.D. Pack, Special points for Brillouin-zone integrations, *Phys. Rev. B* 13 (1976) 5188–5192.

[53] G. Henkelman, H. Jonsson, Improved tangent estimate in the nudged elastic band method for finding minimum energy paths and saddle points, *J. Chem. Phys.* 113 (2000) 9978–9985.

[54] D. Sheppard, G. Henkelman, Paths to which the nudged elastic band converges, *J. Comput. Chem.* 32 (2011) 1769–1771.

[55] Y.-S. Wei, M. Zhang, M. Kitta, Z. Liu, S. Horike, Q. Xu, A single-crystal open-capsule metal–organic framework, *J. Am. Chem. Soc.* 141 (2019) 7906–7916.

[56] X. Hu, G. Luo, Q. Zhao, D. Wu, T. Yang, J. Wen, R. Wang, C. Xu, N. Hu, Ru single atoms on N-doped carbon by spatial confinement and ionic substitution strategies for high-performance Li–O<sub>2</sub> batteries, *J. Am. Chem. Soc.* 142 (2020) 16776–16786.

[57] Z. Jiang, W. Sun, H. Shang, W. Chen, T. Sun, H. Li, J. Dong, J. Zhou, Z. Li, Y. Wang, R. Cao, R. Sarangi, Z. Yang, D. Wang, J. Zhang, Y. Li, Atomic interface effect of a single atom copper catalyst for enhanced oxygen reduction reactions, *Energy Environ. Sci.* 12 (2019) 3508–3514.

[58] Y. Zheng, Y. Jiao, Y. Zhu, L.H. Li, Y. Han, Y. Chen, M. Jaroniec, S.-Z. Qiao, High electrocatalytic hydrogen evolution activity of an anomalous ruthenium catalyst, *J. Am. Chem. Soc.* 138 (2016) 16174–16181.

[59] J.N. Tiwari, A.M. Harzandi, M. Ha, S. Sultan, C.W. Myung, H.J. Park, D.Y. Kim, P. Thangavel, A.N. Singh, P. Sharma, S.S. Chandrasekaran, F. Salehnia, J.-W. Jang, H.S. Shin, Z. Lee, K.S. Kim, Hydrogen evolution: high-performance hydrogen evolution by Ru single atoms and nitrided-Ru nanoparticles implanted on N-doped graphitic sheet, *Adv. Energy Mater.* 9 (2019), 1970101.

[60] C. Wei, R.R. Rao, J. Peng, B. Huang, I.E.L. Stephens, M. Risch, Z.J. Xu, Y. Shao-Horn, Recommended practices and benchmark activity for hydrogen and oxygen electrocatalysis in water splitting and fuel cells, *Adv. Mater.* 31 (2019), 1806296.

[61] J. Wang, F. Xu, H. Jin, Y. Chen, Y. Wang, Non-noble metal-based carbon composites in hydrogen evolution reaction: fundamentals to applications, *Adv. Mater.* 29 (2017), 1605838.

[62] J. Luo, J.H. Im, M.T. Mayer, M. Schreier, M.K. Nazeeruddin, N.G. Park, S.D. Tilley, H.J. Fan, M. Grätzel, Water photolysis at 12.3% efficiency via perovskite photovoltaics and Earth-abundant catalysts, *Science* 345 (2014) 1593–1596.

[63] P. Su, W. Pei, X. Wang, Y. Ma, Q. Jiang, J. Liang, S. Zhou, J. Zhao, J. Liu, G.Q. Lu, Exceptional electrochemical HER performance with enhanced electron transfer between Ru nanoparticles and single atoms dispersed on a carbon substrate, *Angew. Chem. Int. Ed.* 60 (2021) 16044–16050.

[64] C.-F. Li, J.-W. Zhao, L.-J. Xie, Y. Wang, H.-B. Tang, L.-R. Zheng, G.-R. Li, N coupling with S-coordinated Ru nanoclusters for highly efficient hydrogen evolution in alkaline media, *J. Mater. Chem. A* 9 (2021) 12659–12669.

[65] D. Voiry, M. Chhowalla, Y. Gogotsi, N.A. Kotov, Y. Li, R.M. Penner, R.E. Schaak, P. S. Weiss, Best practices for reporting electrocatalytic performance of nanomaterials, *ACS Nano* 12 (2018) 9635–9638.

[66] Y. Xu, C. Wang, Y. Huang, J. Fu, Recent advances in electrocatalysts for neutral and large-current-density water electrolysis, *Nano Energy* 80 (2021), 105545.

[67] S. Niu, W.-J. Jiang, Z. Wei, T. Tang, J. Ma, J.-S. Hu, L.-J. Wan, Se-doping activates FeOOH for cost-effective and efficient electrochemical water oxidation, *J. Am. Chem. Soc.* 141 (2019) 7005–7013.